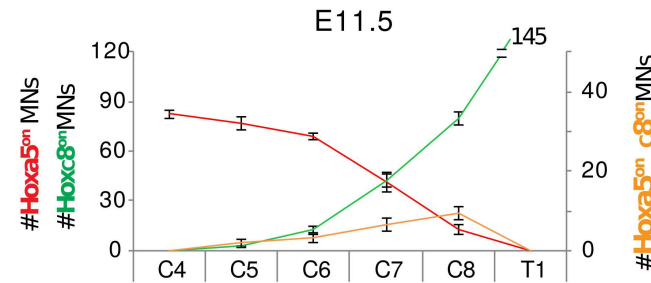
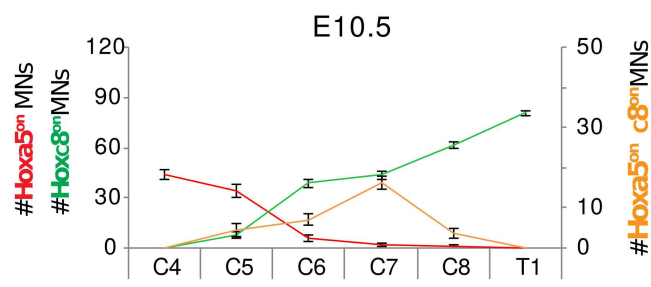
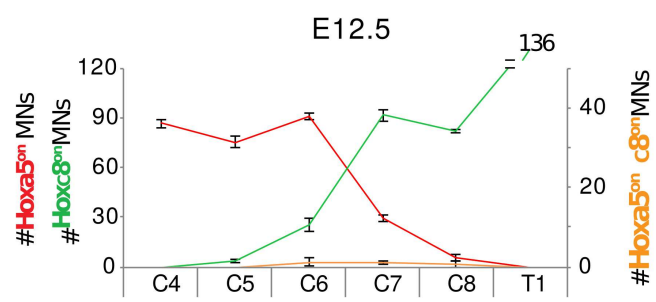
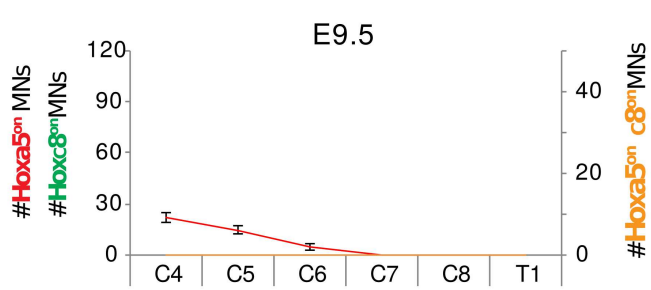
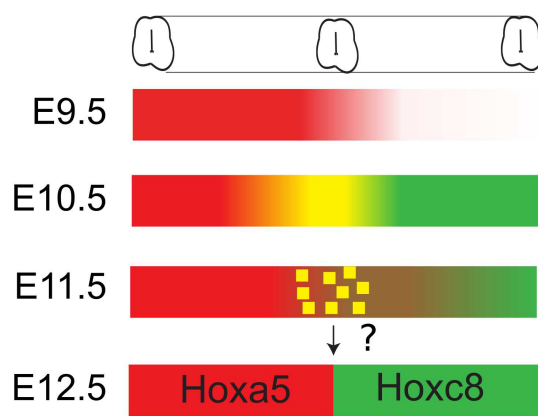
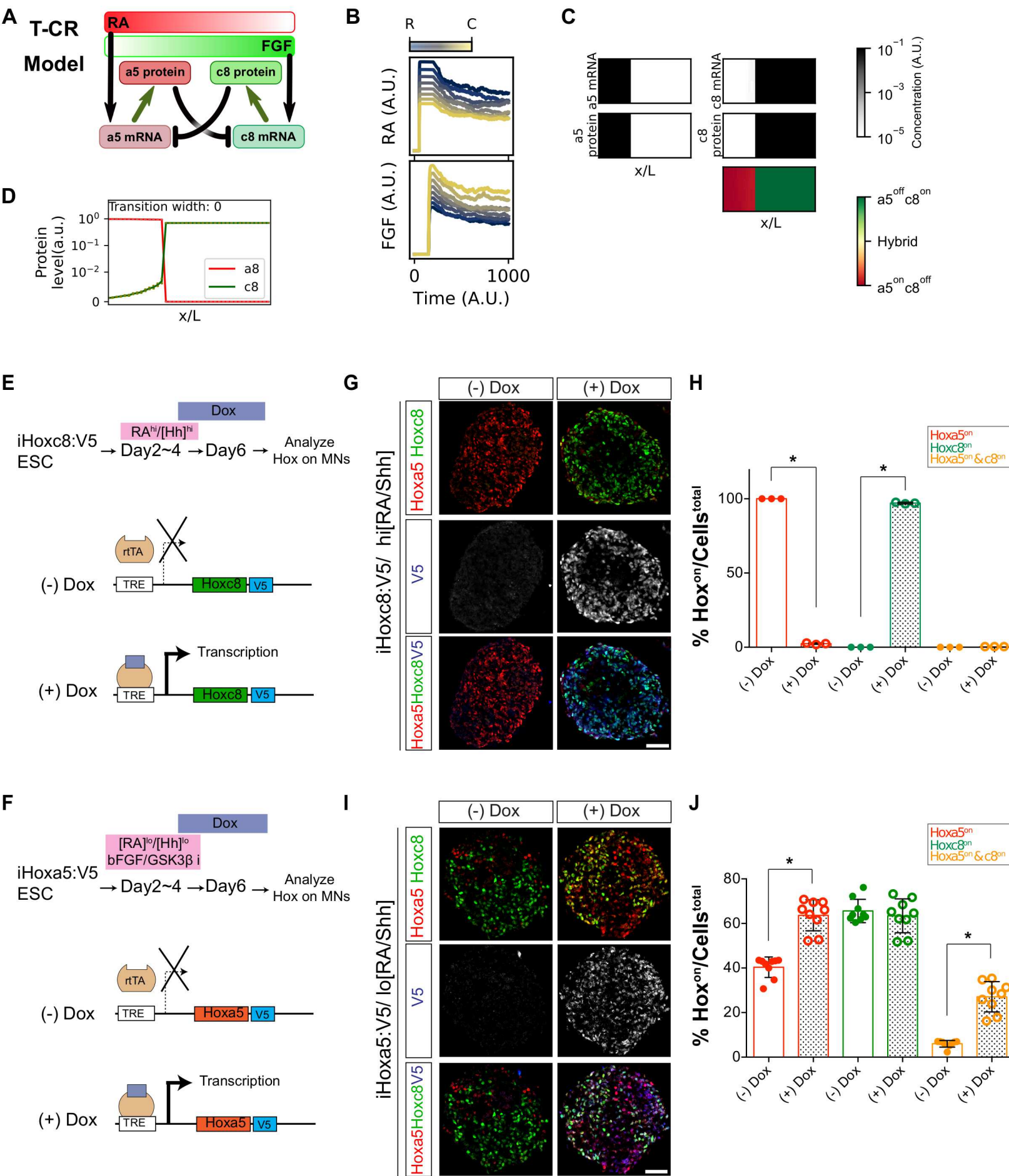
**B****C****Cervical**

**Figure 1. Lineage segregation of Hoxa5/Hoxc8-expressing cells in the developing spinal cord.**

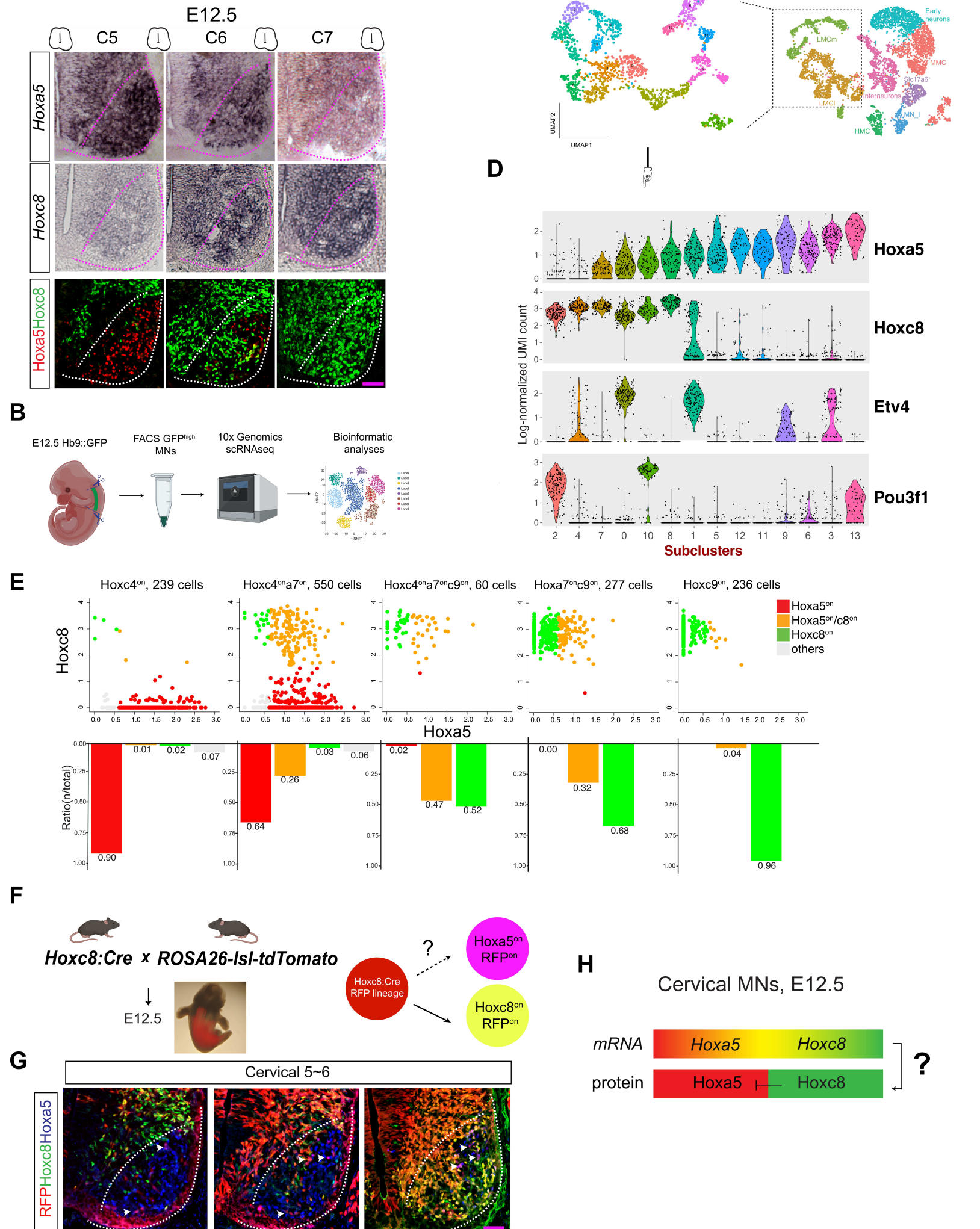
(A) Expression patterns of Hoxa5 and Hoxc8 in MNs (demarcated by white dashed lines) along the rostrocaudal axis of the spinal cord (cervical C4 to thoracic T1) from mouse embryos from E9.5 to E12.5. Pink scale bars: 12.5  $\mu$ m for E9.5; 12.5  $\mu$ m for E10.5; 25  $\mu$ m for E11.5; and 50  $\mu$ m for E12.5. (B) Quantification of Hox<sup>on</sup> cells across MN domains. Data represent mean  $\pm$  SD from  $N \geq 3$  embryos. (C) Summary of the intrasegmental expression profiles of Hoxa5 and Hoxc8 in cervical MNs.

Figure 2

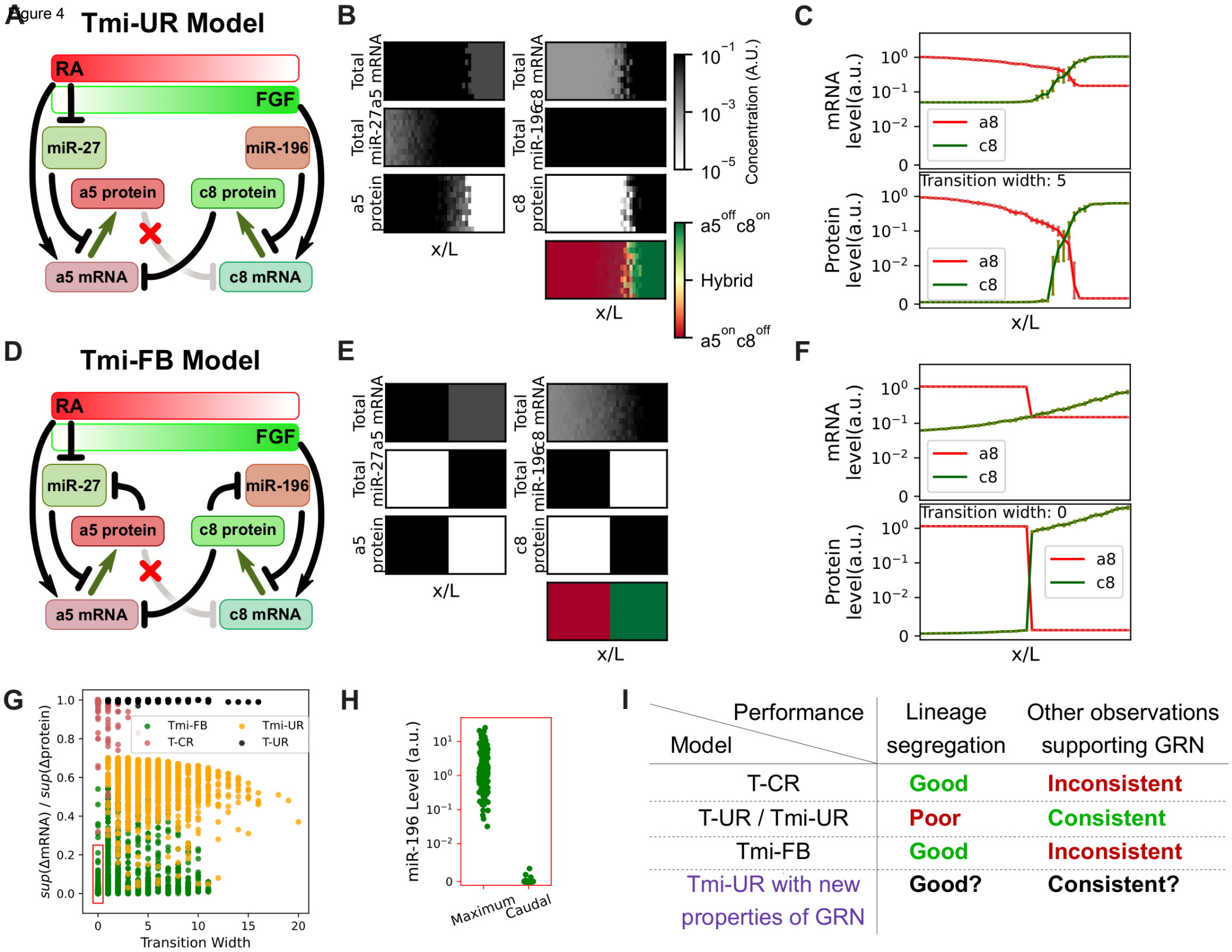


**Figure 2. Cross-repressive loop is not applicable in the Hoxc8-Hoxa5 lineage segregation in spinal motor neurons.** (A) Schematic of the transcriptional cross-repression model (T-CR Model). (B) Presumptive simulated time-course of RA and FGF signaling at multiple locations along the rostrocaudal (RC) axis. A.U.: arbitrary unit. (C) Simulation of the T-CR Model. A grid of 10X40 cells was used to represent a segment of developing spinal cord where progenitor cells are influenced by competing FGF and RA concentrations. Heatmaps reflect final distributions of denoted molecules in the tissue domain. Bottom panel shows the distribution of the ratios between Hoxa5 and Hoxc8 protein levels. (D) Steady state levels of Hoxa5 and Hoxc8 proteins across RC domains. Error bar indicates 95% confidence interval for each position receiving the same amount of morphogen. Transition width is defined as number of positions where one or more cells have equivocal lineage decision. (E and F) Schematic illustrations of the design of inducible “Tet-On” ESC lines expressing Hoxa5 or Hoxc8 under the doxycycline (Dox)-regulated promoter. In the presence of Dox, the reverse tTA (rtTA) activator is recruited to the TRE (Tetracycline Response Element), thereby initiating transcription of the downstream gene. (G and I) Immunostaining reveals expression of Hoxa5 and Hoxc8 upon induction of exogenous Hoxc8:V5 (iHoxc8:V5) or Hoxa5:V5 (iHoxa5:V5), respectively. (H and J) Quantification of data from G and I (mean  $\pm$  SD, N $\geq$ 3 EBs from three independent experiments, \*p < 0.01). Scale bars in G and I represent 50  $\mu$ m.

Figure 3



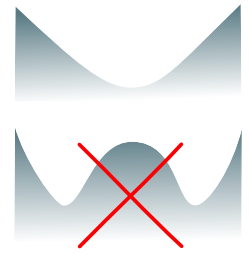
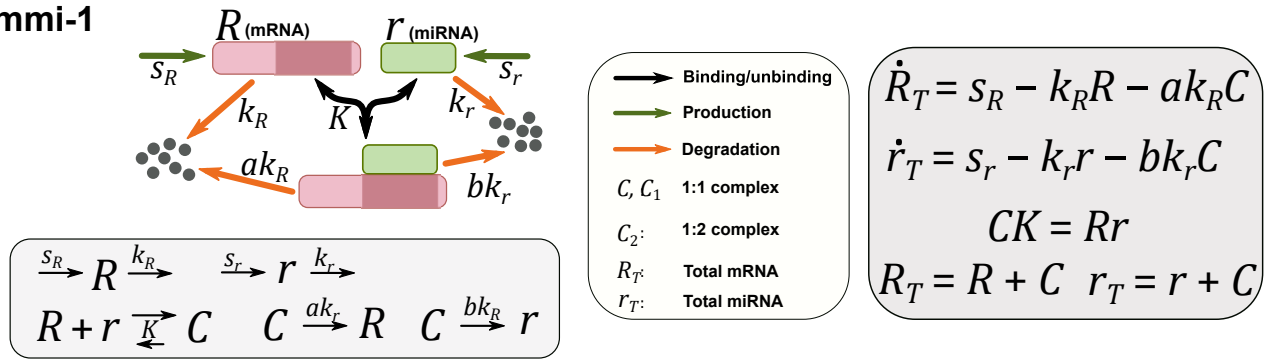
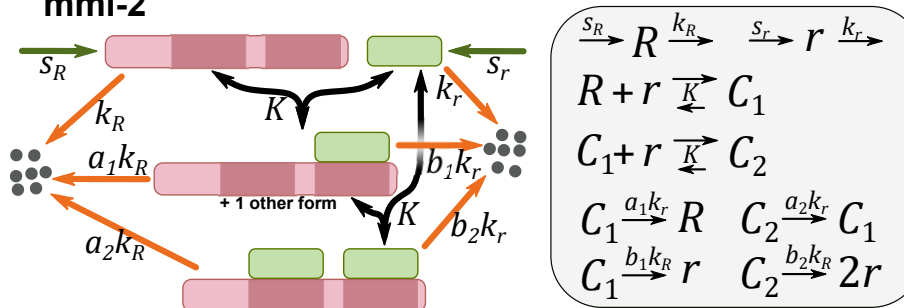
**Figure 3. Single-cell RNAseq and lineage tracing indicate coexistence of *Hoxa5/Hoxc8* mRNAs in MNs along the spinal cord.** (A) Expression patterns of *Hoxa5* and *Hoxc8* mRNAs, as revealed by *in situ* hybridization, aligned with corresponding sections showing Hoxa5 and Hoxc8 immunostainings in MNs (demarcated with pink/white dashed lines) along the cervical spinal cord (cervical C5 to C7) in mouse embryos at E12.5. Pink scale bar, 50  $\mu$ m. (B) Schematic illustration of the strategy to apply single-cell RNA sequencing (scRNAseq) on FACS-collected homogenous Hb9:GFP<sup>on</sup> MNs. (C) Visualization of E12.5 cervical MNs (right panel) and the subset of LMCs (left panel) using Uniform Manifold Approximation and Projection (UMAP), a 2D non-linear transformation of high-dimensional data that assigns proximal x-y coordinates to cells (points) with similar expression profiles. Individual cells are colored according to their cluster assignments. Details are provided in the Materials & Methods. (D) Dot-plots showing expression of genes (rows) that distinguish MN subtypes (columns). The height of each colored shape is proportional to the percentage of cells expressing the marker ( $\geq 1$  UMI), and its width reflects the average transcript count within expressing cells. (E) scRNAseq results reflect that *Hoxa5/Hoxc8* mRNAs largely co-exist along the RC axis of E12.5 spinal cord, particularly at the middle boundary region. (F) Schematic illustration of Hoxc8 lineage tracing. *Hoxc8*-expressing cells and all of their progeny are indelibly marked by tdTomato (RFP) expression in *Hoxc8:Cre;ROSA26-loxp-STOP-loxp-tdTomato (lsl-tdTomato)* embryos. (G) Analysis of the Hoxc8 lineage (RFP<sup>on</sup> cells) in *Hoxc8:Cre;ROSA26-lsl-tdTomato* E12.5 spinal cord sections (cervical segments 5-6). RFP is expressed in a broad domain that includes Hoxc8<sup>on</sup> cells and a subset of Hoxa5<sup>on</sup> cells (Hoxa5<sup>on</sup> plus RFP<sup>on</sup>, indicated by arrowheads). Pink scale bar, 50  $\mu$ m. (H) Hoxa5<sup>on</sup> and Hoxc8<sup>on</sup> cells adopt an “all or none” segregated cell fate despite coexistence of *Hoxa5/Hoxc8* mRNAs, indicating a potential post-transcriptional regulatory mechanism for cell fate segregation.



**Figure 4. Two alternative models of miRNA-mediated regulation.** (A) Schematic of the model representing transcriptional unilateral repression with miRNA-mediated regulation (Tmi-UR Model). (B) Simulation of the Tmi-UR Model. A grid of 10X40 cells was used to represent a segment of developing spinal cord where progenitor cells are influenced by competing FGF and RA concentrations. Heatmaps show the final distributions of denoted molecules in the tissue domain. Bottom panel shows the distribution of ratios between Hoxa5 and Hoxc8 protein levels. (C) Steady state levels of *Hoxa5* and *Hoxc8* mRNA (top) and proteins (bottom) across RC domains under Tmi-UR Model. Error bar indicates 95% confidence interval for each position receiving the same amount of morphogen. (D) Schematic of the model representing transcriptional unilateral repression with miRNA-mediated feedback (Tmi-FB Model). Hypothetical mRNA-miRNA feedback involving transcriptional repression of miRNA by target mRNA is assumed. (E) Simulation of the Tmi-FB Model. A grid of 10X40 cells was used to represent a segment of developing spinal cord where progenitor cells are influenced by competing FGF and RA concentrations. Heatmaps show final distributions of denoted molecules in the tissue domain. Bottom panel shows the distribution of ratios between Hoxa5 and Hoxc8 protein levels. (F) Steady state levels of *Hoxa5* and *Hoxc8* mRNA (top) and proteins (bottom) across RC domains under Tmi-FB Model. Error bar indicates 95% confidence interval for each position receiving the same amount of morphogen. (G) Performance of 3000 top performing parameter sets from randomly generated values for each model (SI Table S3). y-coordinates are mRNA-to-protein ratios in terms of the gradient steepness along the RC axis (segregation index, see SI Text for details). Red square indicates selected 190 sets (100% from Tmi-FB) for further analysis. (H) Quantifications of steady state *miR-196* levels for models selected from G. Caudal boundary level is compared to maximum

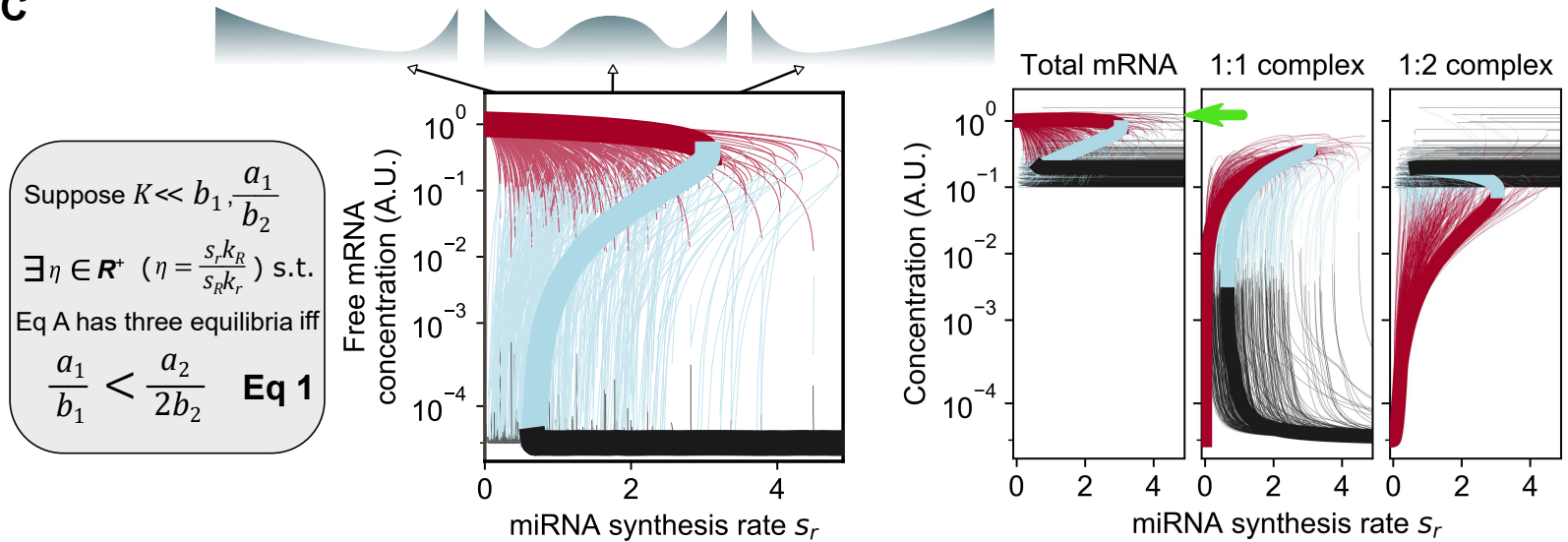
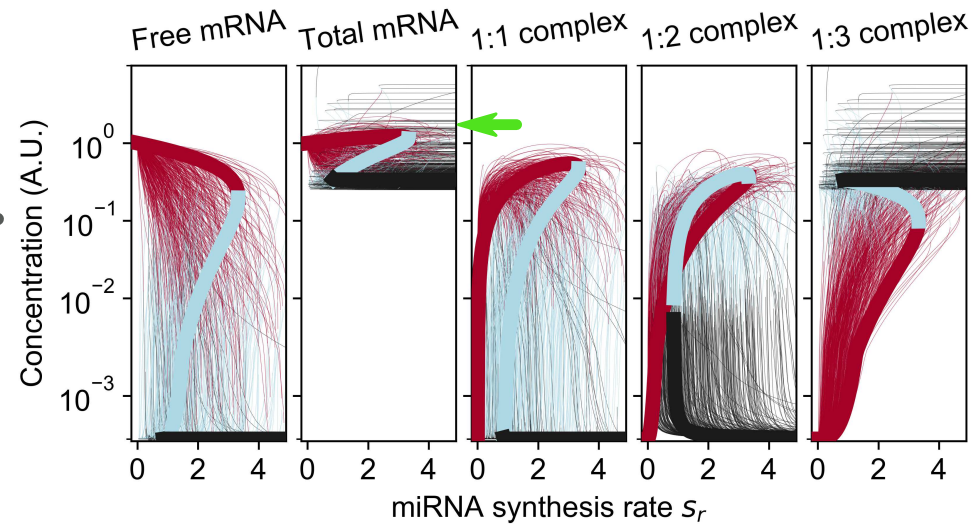
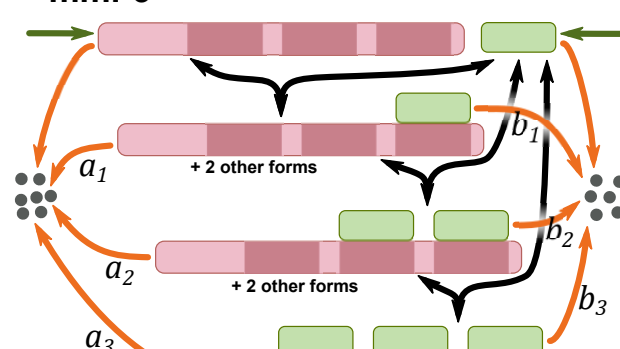
level across the RC domain. (I) Summary of lineage decision performance and consistency with experimental data for four models.

Figure 5

**A mmi-1****B mmi-2**

$$\begin{aligned}\dot{R}_T &= s_R - k_R(R + a_1 C_1 + a_2 C_2) \\ \dot{r}_T &= s_r - k_r(r + b_1 C_1 + b_2 C_2) \\ KC_1 &= Rr \quad R_T = R + 2C_1 + C_2 \\ KC_2 &= C_1 r \quad r_T = r + 2C_1 + 2C_2\end{aligned}$$

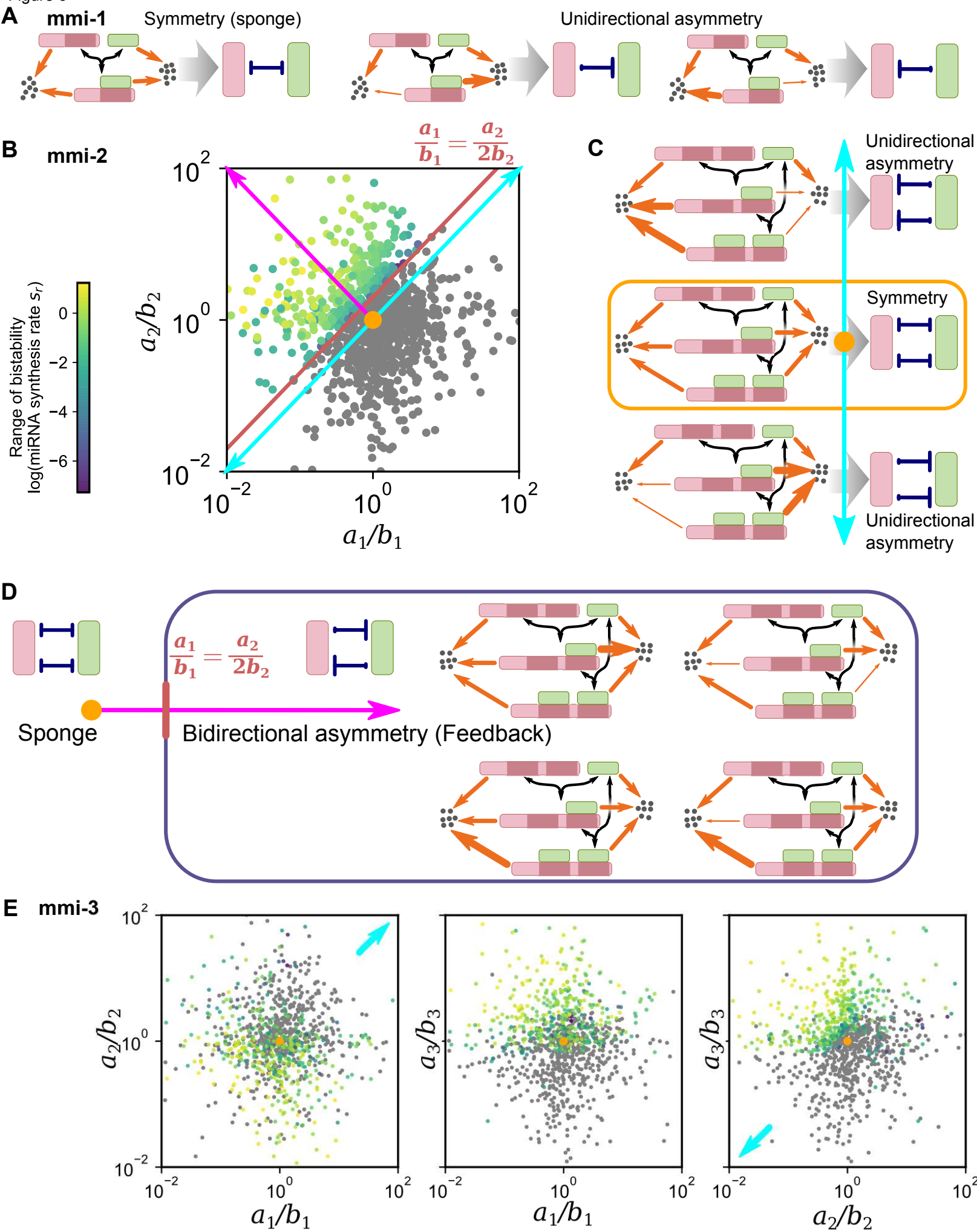
Eq A

**C****D mmi-3**

**Figure 5. Models for cell fate decisions governed by mRNA-miRNA reaction networks. (A)**

An mRNA-miRNA reaction network with one miRNA binding site on the target mRNA (mmi-1 Model). (B) An mRNA-miRNA reaction network with two miRNA binding sites on the target mRNA (mmi-2 Model). In A and B, light gray boxes show chemical reactions and rate constants, whereas dark gray boxes show the differential-algebraic equations (DAEs) that describe the dynamics of all molecular species. (C) Gray box indicates the condition that allows bistability (with Eq A depicted in panel B). We generated 10000 parameter sets, with values for  $a_1$ ,  $a_2$ ,  $b_1$  and  $b_2$  randomly drawn from a uniform distribution over the interval (0.125, 16). All other parameters, except the control parameter for bifurcation analysis and the scaled dissociation rate constant ( $Kk_R^0/s_R = 10^{-5}$ ), were set to 1. Bifurcation diagrams demonstrate the steady states calculated for 3348 bistable systems out of 10000 parameter sets. Red curve: stable steady state with high amounts of free mRNA. Black curve: stable steady state with low amounts of free mRNA. Blue curve: unstable steady state. One representative system is highlighted with thick curves, and other systems are represented by thin curves. (D). Left: mRNA-miRNA reaction network with three miRNA binding sites on the target mRNA (mmi-3 Model). Right: bifurcation analysis performed as described in (C). Of 10000 parameter sets, 5081 gave rise to bistable systems. Light green arrows in the bifurcation plots of (C) and (D) denote parameter sets in which mRNA degradation is not enhanced by complex formation. In these systems, a steady state is established in the presence of high amounts of miRNA but with total mRNA levels not less than 1.

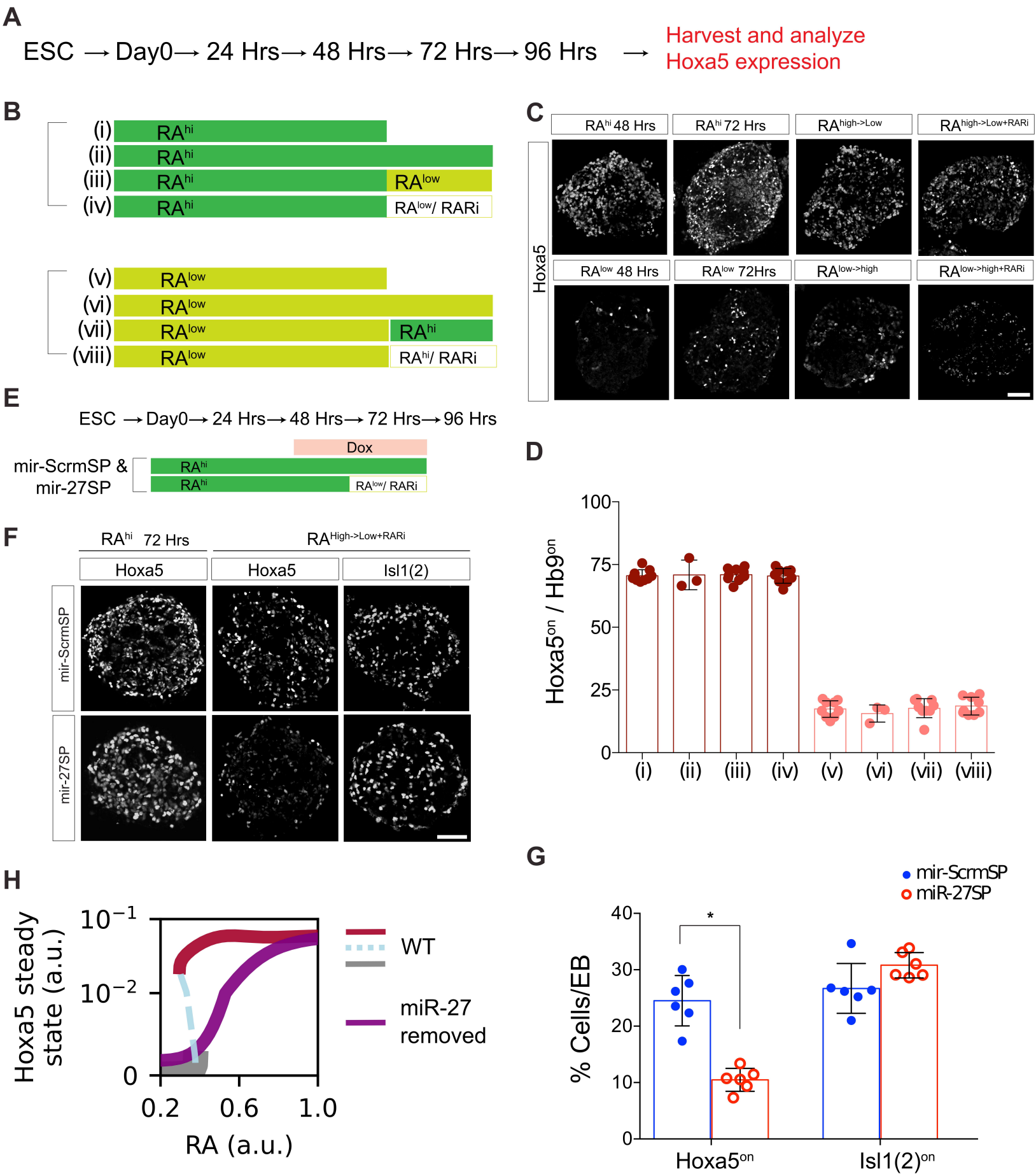
Figure 6



**Figure 6. Theoretical framework for the bistability conditions of mRNA-miRNA reaction networks.** (A) Conversion of the mmi-1 Model reaction network into influence diagrams based on two assumptions of kinetics. Left: symmetrical inhibition governed by balanced degradation rate constants in the complex. Right: asymmetrical and unidirectional inhibition governed by unbalanced degradation rate constants between mRNA and miRNA in the complex. Red: mRNA; Green: miRNA. (B) Stability properties of 10000 randomly generated mmi-2 Model systems based on the procedure described in the legend to Figure 5C. Monostable systems (gray dots) and bistable systems (purple-green dots) are shown in the dimensions for  $a_1/b_1$  and  $a_2/b_2$ . The color gradient denotes the range of bistability in terms of the control parameter. Orange dot denotes the condition under which degradation of mRNA and miRNA is balanced in both complexes. Red line is the threshold for bistability predicted by analytical methods. Cyan and magenta arrows serve as visual guides for panels C and D. (C) Schematic depicting that when both complexes favor the same RNA species (mRNA or miRNA) with unbalanced degradation rate constants, the influences of mRNA and miRNA on each other are asymmetrical and unidirectional. (D) Schematic depicting a spectrum of influences from sponge-like inhibition to feedback-like mutual inhibition. When two complexes favor different RNA species with unbalanced degradation rate constants, the influences of mRNA and miRNA on each other can become asymmetrical and bidirectional, forming a feedback loop. Four examples of the kinetic relationships (degradation rate constants) are shown in the box at right. (E) Stability properties of 10000 randomly generated systems reflecting the mmi-3 Model based on the procedure described in the legend to Figure 5C. Monostable systems (gray dots) and bistable systems (purple-green dots) are shown in the dimensions for  $a_1/b_1$ ,  $a_2/b_2$  and  $a_3/b_3$ . Color gradient denotes the range of bistability in terms of the control parameter. Orange dot denotes the condition under which degradation of mRNA and miRNA is balanced in

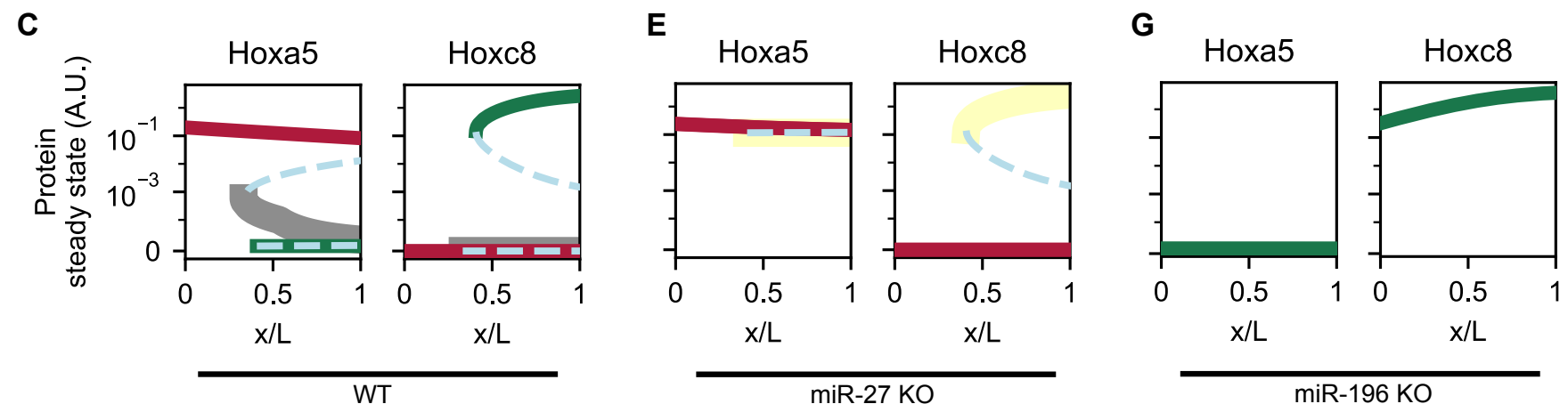
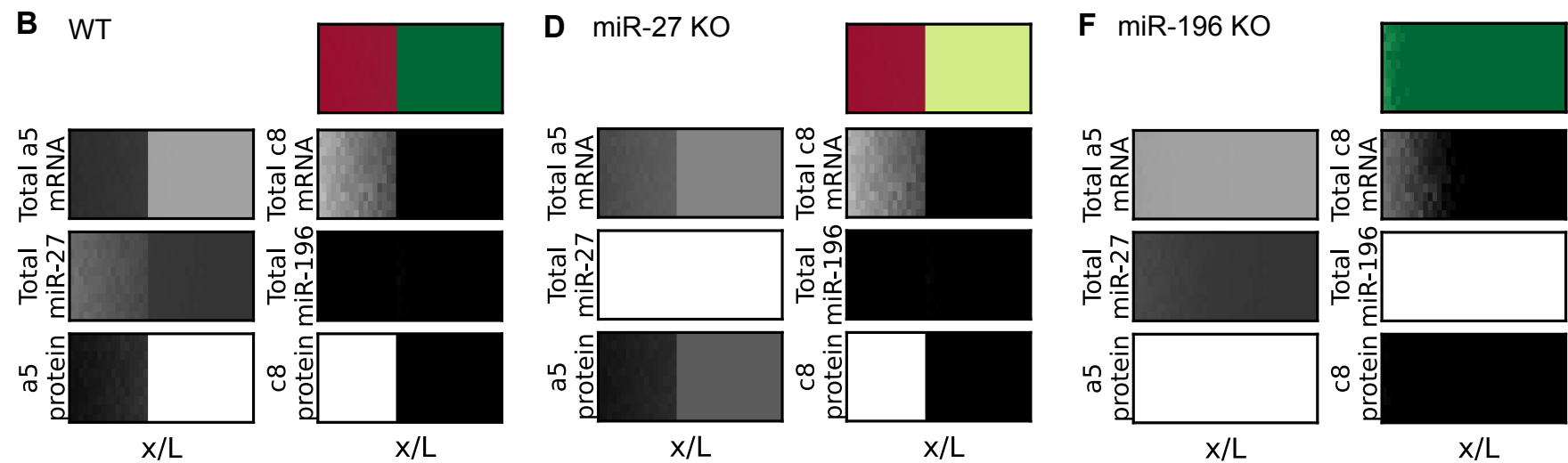
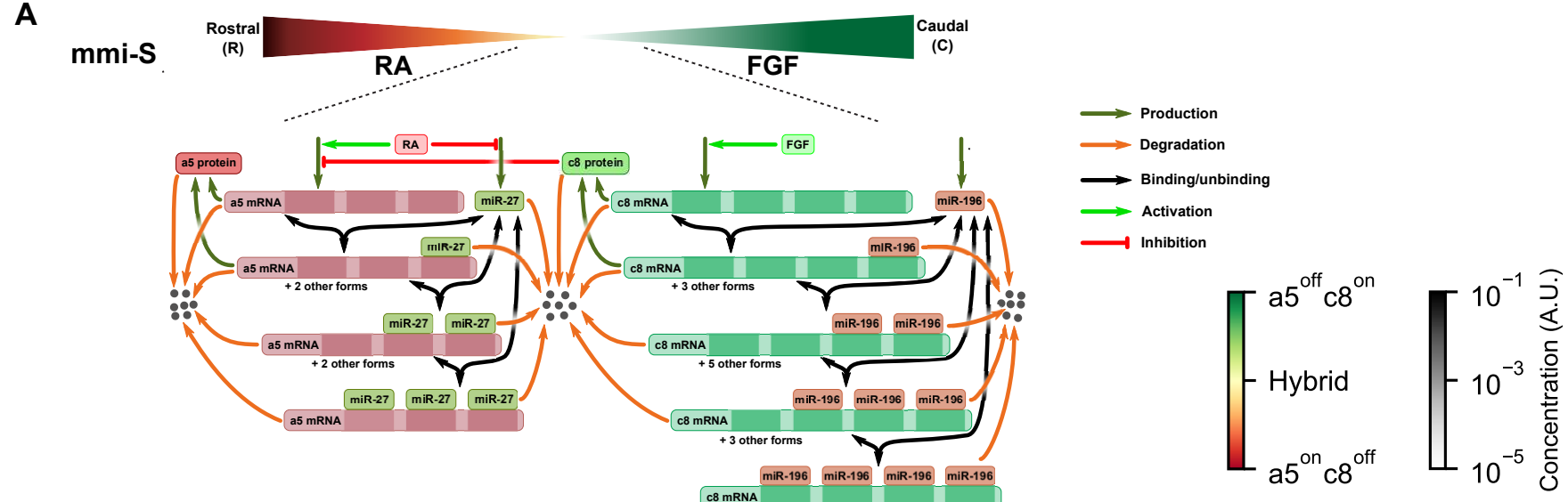
the three complexes. Cyan arrows denote the parameter regions in which unidirectional asymmetry of the inhibitions only gave rise to monostable systems (left plot: complexes favor miRNA-mediated mRNA degradation; right plot: complexes favor mRNA-mediated miRNA degradation).

Figure 7



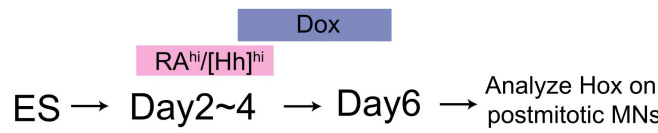
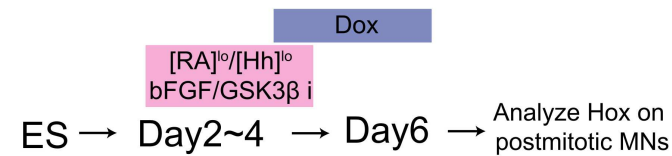
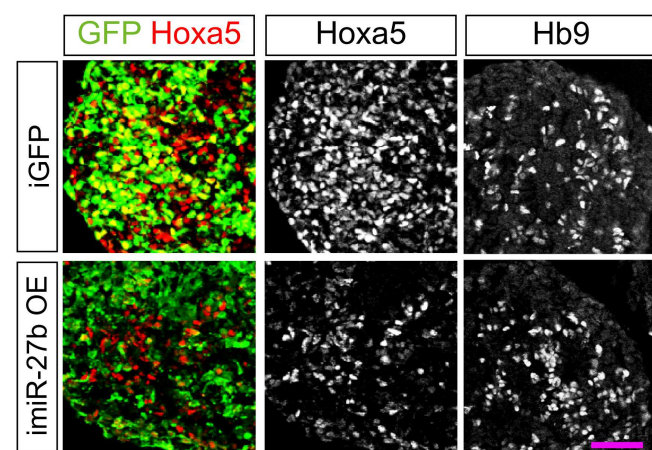
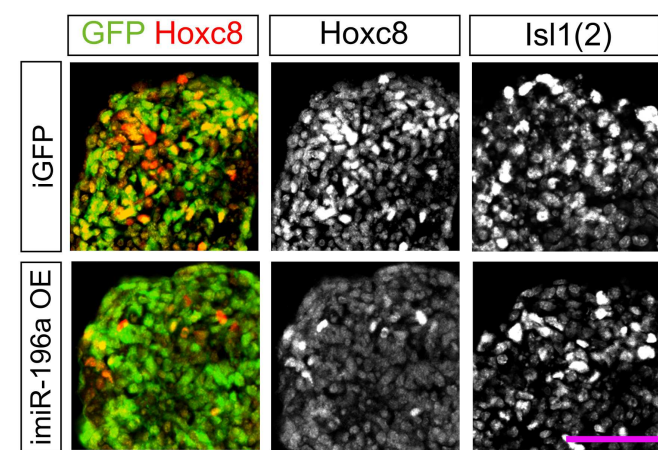
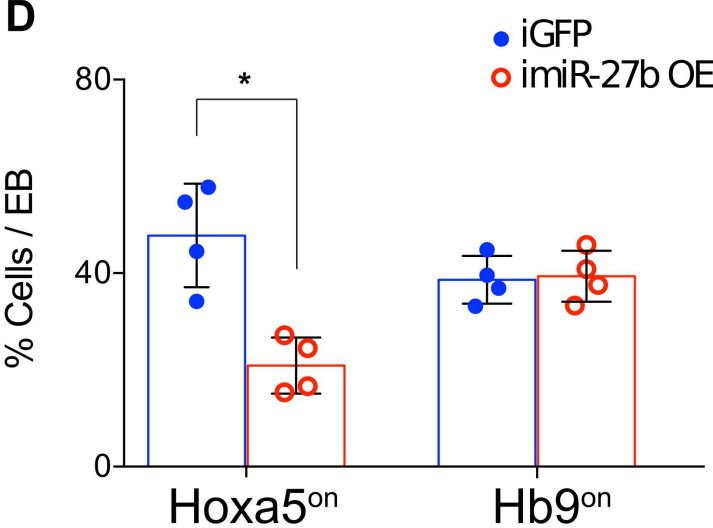
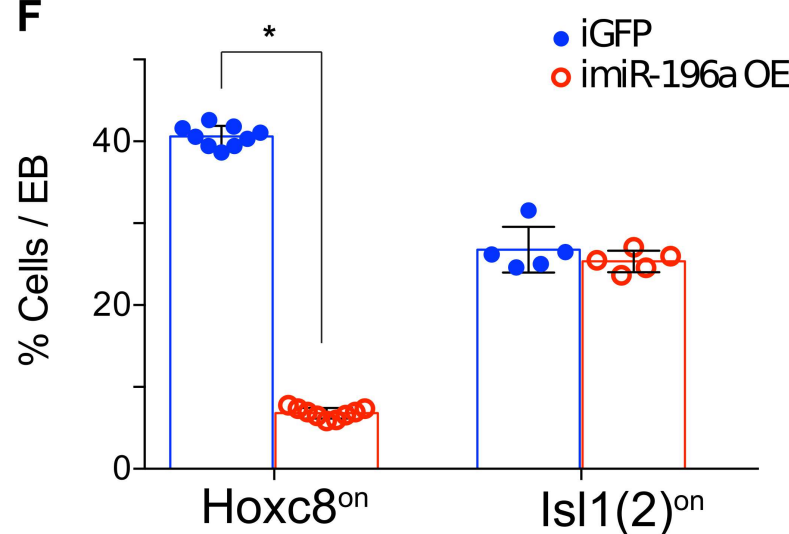
**Figure 7. miRNA confers hysteresis in MN differentiation.** (A and B) Schematic illustrations of the experiments in (C) and (D). Embryoid bodies were incubated with: (i) RA<sup>hi</sup> (1  $\mu$ M) for 48 h; (ii) RA<sup>hi</sup> for 72 h; (iii) RA<sup>hi</sup> for 48 h then switched to RA<sup>low</sup> (100 nM) for 24 h; (iv) RA<sup>hi</sup> for 48 h then switched to RA<sup>low</sup> plus RAR inhibitor (1  $\mu$ M) for a further 24 h; (v) RA<sup>low</sup> for 48 h; (vi) RA<sup>low</sup> for 72 h; (vii) RA<sup>low</sup> for 48 h then switched to RA<sup>hi</sup> for a further 24 h; or (viii) RA<sup>low</sup> for 48 h then switched to RA<sup>hi</sup> plus RAR inhibitor (1  $\mu$ M) for 24 h. Immunostaining (C) of EBs 96 h after ESC differentiation, and quantification (D) of Hoxa5<sup>on</sup> in MNs (Hb9<sup>on</sup>). Scale bar in (C) represents 50  $\mu$ m. Data in (D) represent mean  $\pm$  SD, N $\geq$ 3 EBs from three independent experiments, \*p < 0.01. (E) Schematic illustration of the experiments in (F) and (G). Inducible ESC lines expressing eight repetitive *mir-27b* sponge sequences were inserted into the GFP 3' UTR. ESCs were differentiated by doxycycline treatment after 48 h of differentiation. A scrambled sequence was inserted as a control. (F and G) Hoxa5 expression is compromised upon *miR-27* knockdown, exposure to RA<sup>hi</sup> for 48 h and then switching to RA<sup>low</sup> plus RAR inhibitor (1  $\mu$ M) for a further 24 h. Scale bar in (F) represents 50  $\mu$ m. Data in (G) represents mean  $\pm$  SD, N $\geq$ 3 EBs from three independent experiments, \*p < 0.01. (H) Bifurcation analysis of a mathematical model based on our mmi-3 Model. Steady states of the system in the presence of *miR-27* (red, gray, and blue) or in the absence of *miR-27* (purple) at various concentrations of RA are shown. Solid curve: stable steady state. Dashed curve: unstable steady state (See SI Text for parameter values).

Figure 8



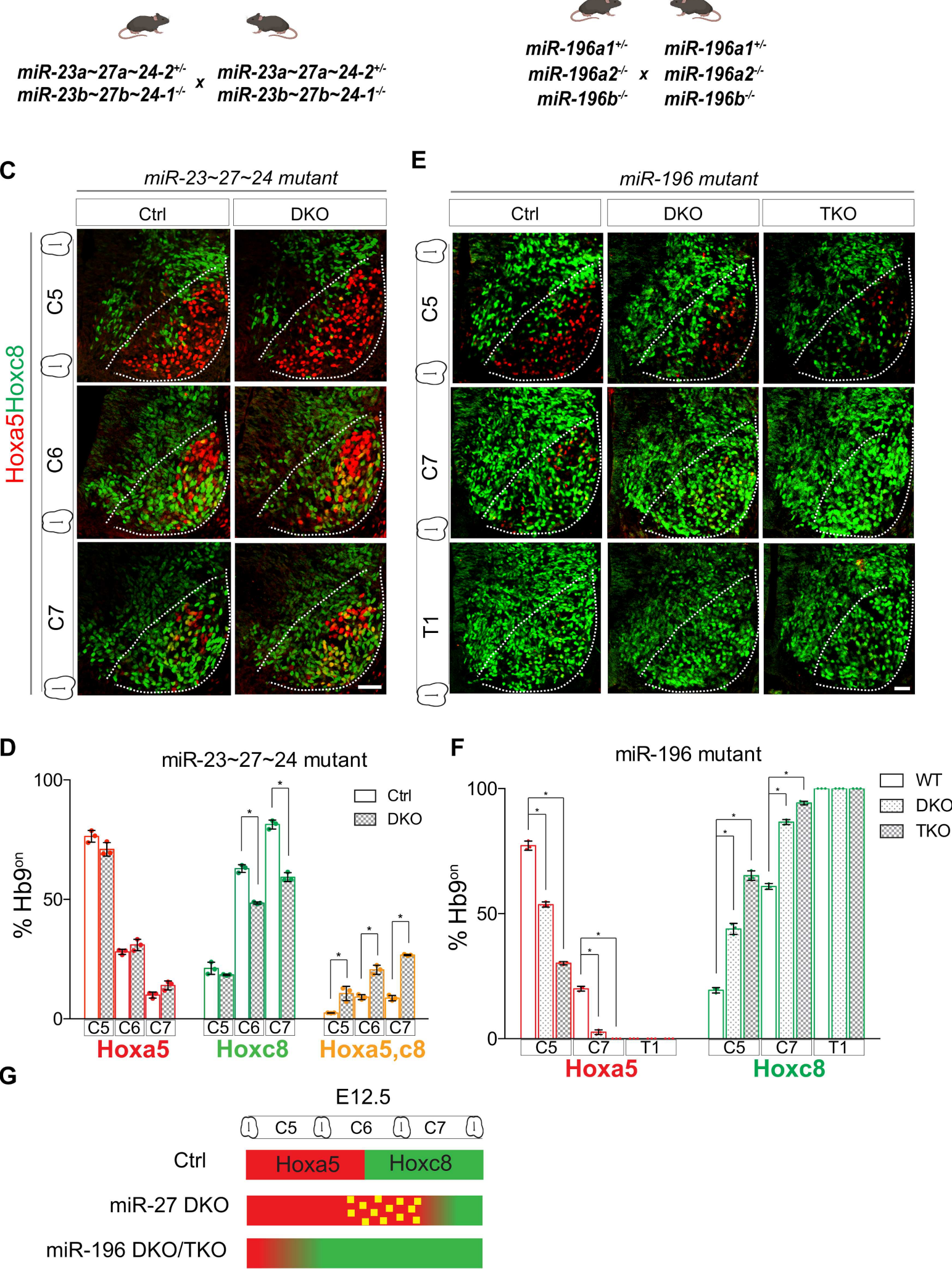
**Figure 8. Spatiotemporal model for rostrocaudal patterning of MN development.** (A) Reaction network for MN development in the RC axis of the spinal cord. Cellular-level reactions including mRNA-miRNA interactions contain known binding sites of *miR-27* and *miR-196* on the 3' UTRs of the *Hoxa5* and *Hoxc8* mRNAs, respectively. RA and FGF act as signaling molecules to influence transcription. (B) Simulation of the spatiotemporal model. A grid of 10X40 cells was used to represent a segment of developing spinal cord where progenitor cells are influenced by competing FGF and RA concentrations. Panel at top right shows the distribution of ratios between *Hoxa5* and *Hoxc8* protein levels. (C) Bifurcation analysis with position as the control parameter. Solid curves denote stable steady states. Gray: *Hoxa5*<sup>off</sup> *Hoxc8*<sup>off</sup> state; Red: *Hoxa5*<sup>on</sup> *Hoxc8*<sup>off</sup> state; Green: *Hoxa5*<sup>off</sup> *Hoxc8*<sup>on</sup> state; The identities of these states were determined by protein levels. Dashed curves denote unstable steady states. (D) Simulation of the spatiotemporal model in the absence of *miR-27*. (E) Bifurcation analysis under the *miR-27* knockout condition. Yellow: hybrid state. (F) Simulation of the spatiotemporal model in the absence of *miR-196*. (G) Bifurcation analysis under the *miR-196* knockout condition. Heatmaps in top right corner show the final distributions of denoted molecules in the tissue domain for panels (B), (D) and (F). Panels (C), (E) and (G) show results for low (final) concentrations of RA and FGF (as shown in Figure 2B).

Figure 9

**A****B****C****E****D****F**

**Figure 9. Overexpression of *miR-27* and *miR-196* leads to the efficient repression of Hoxa5 and Hoxc8 in spinal MNs.** (A and B) Schematic illustrations of the generation of inducible ESC lines expressing primary miRNA sequences inserted into the GFP 3' UTR. ESCs were differentiated under conditional MN differentiation conditions with doxycycline treatment on Day 4 of differentiation. (C-F) Expression of Hoxa5/Hoxc8 and Hb9/Isl1 in EBs from control (iGFP) and iMir-27b- or iMir-196a-overexpressing (OE) cells. Induction of *miR-27b* on Day 4 of differentiation under RA/SAG conditions resulted in reduced Hoxa5 levels (D), whereas induction of *miR-196a* repressed Hoxc8 expression (F). Both conditions have no discernible effect on MN differentiation, as revealed by Hb9 or Isl1 expression (D and F). Pink scale bar in (C) and (E) represents 50  $\mu$ m. Data in (D) and (F) represent mean  $\pm$  SD, N $\geq$ 3 EBs from three independent experiments, \*p < 0.01.

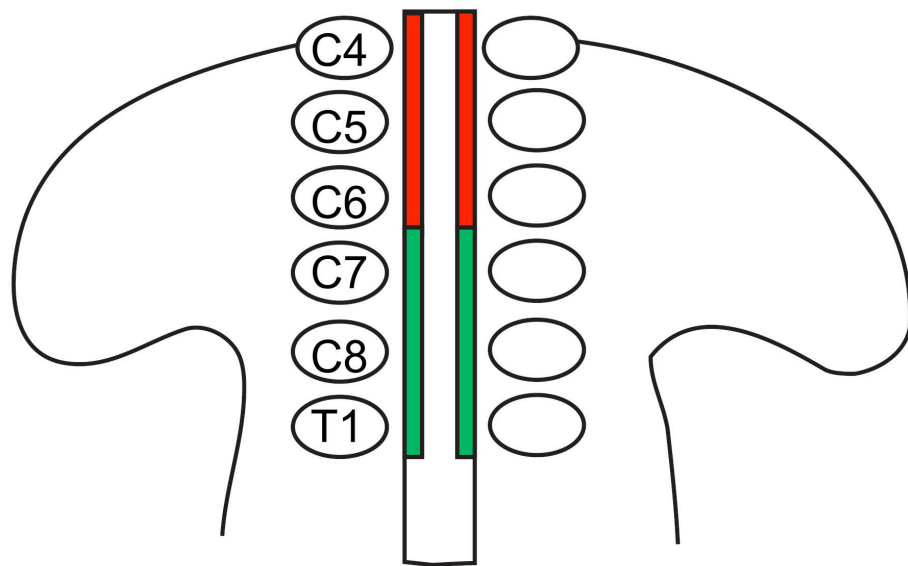
Figure 10



**Figure 10. *miR-27* and *miR-196* mutants manifest a switched Hox boundary in MNs.** (A and B) Schematic illustration of the strategy to generate *miR-27* and *miR-196* knockout embryos. (C~F) (C) Immunostaining at cervical spinal cord sections reveals Hoxa5 expansion into the MNs of cervical C6/7 segments of *miR-23a~27a~24* double KO (DKO) mice. *miR-23a~27a~24-2<sup>+/-</sup>*; *miR-23b~27b~24-1<sup>-/-</sup>* mice were used as a control (ctrl). (E) Conversely, Hoxc8 is shifted into the MNs of cervical C5 segments of both miR-196a2/b DKO and miR-196a1/a2/b triple knockout (TKO) embryos. Age-matched wild type embryos were used as controls. Scale bar represents 50  $\mu$ m. (D and F) Quantifications of Hoxa5<sup>on</sup>, Hoxc8<sup>on</sup>, and Hoxa5<sup>on</sup> Hoxc8<sup>on</sup> cells in the cervical spinal cord of control and knockout embryos (mean  $\pm$  SD, N=3 embryos, \*p < 0.01). (G) Summary of the Hox phenotypes in the miRNA mutants.

Figure S1

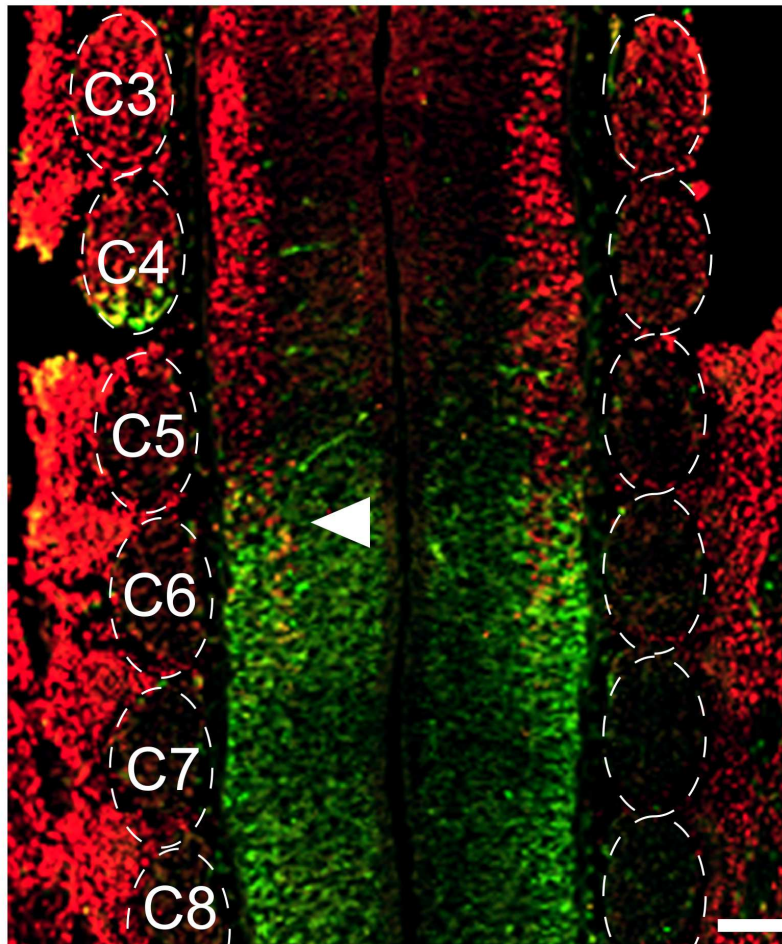
A



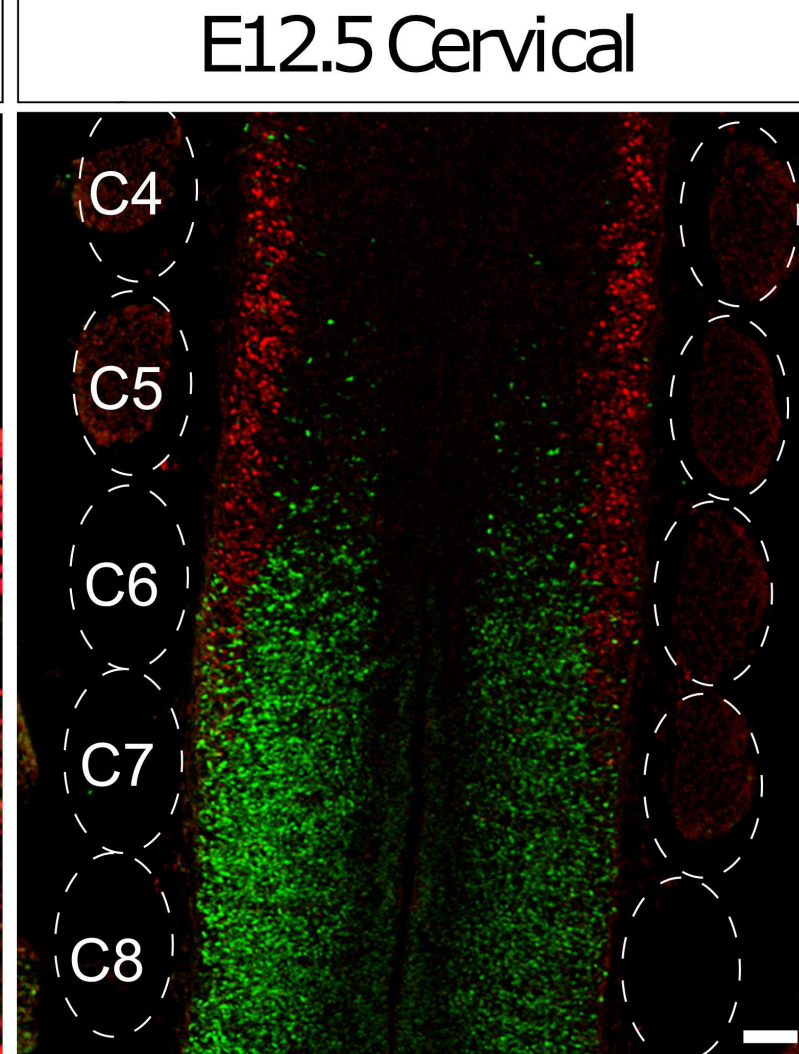
B

## *Hoxa5**Hoxc8*

E11.5 Cervical



E12.5 Cervical

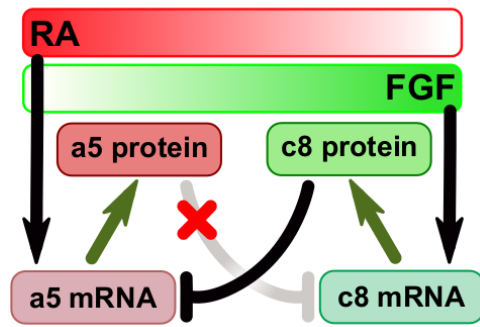
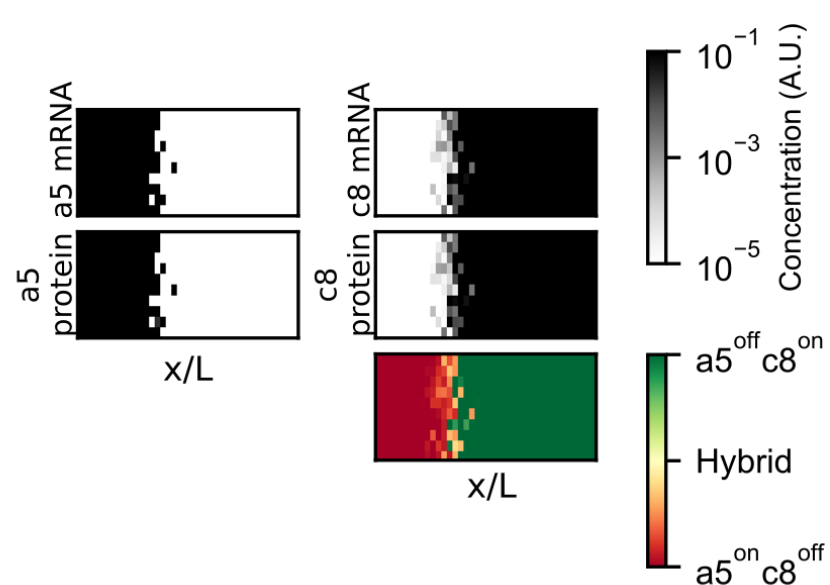
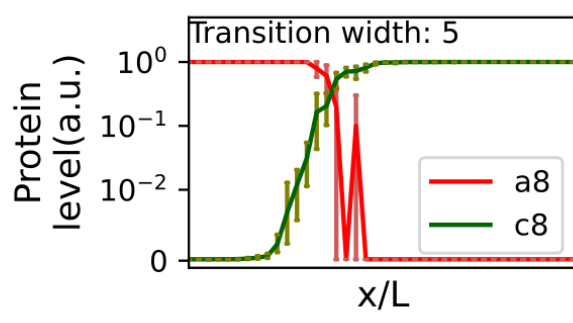
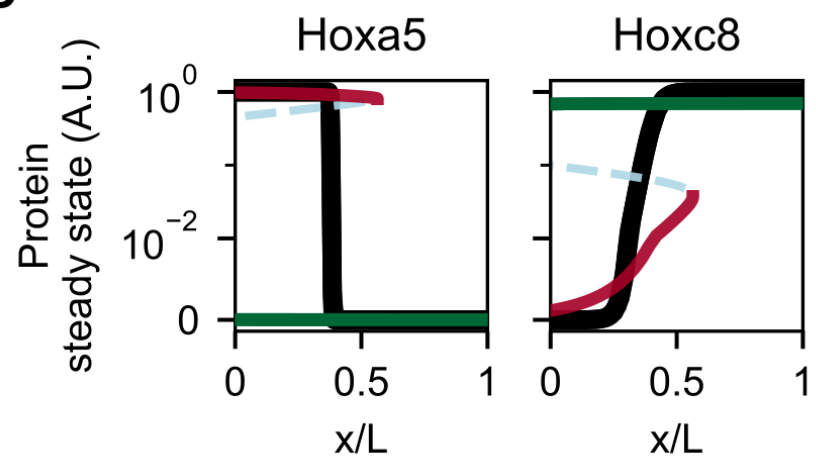
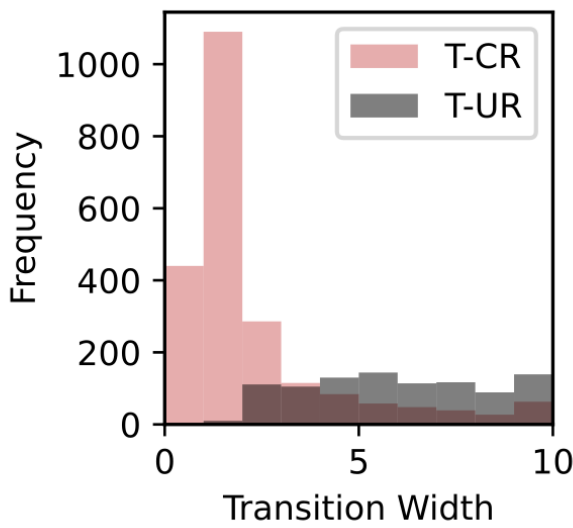
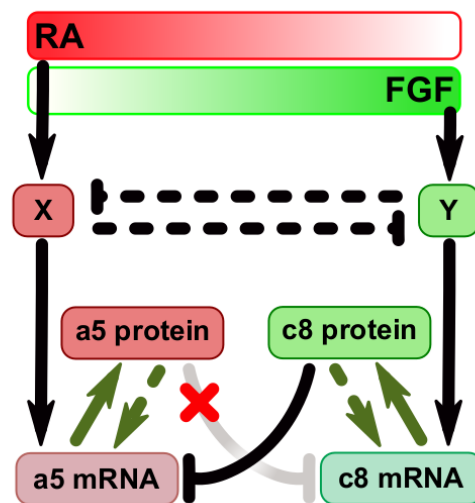


**Figure S1. Expression of Hoxa5 and Hoxc8 along the rostrocaudal axis of the spinal cord. (A)**

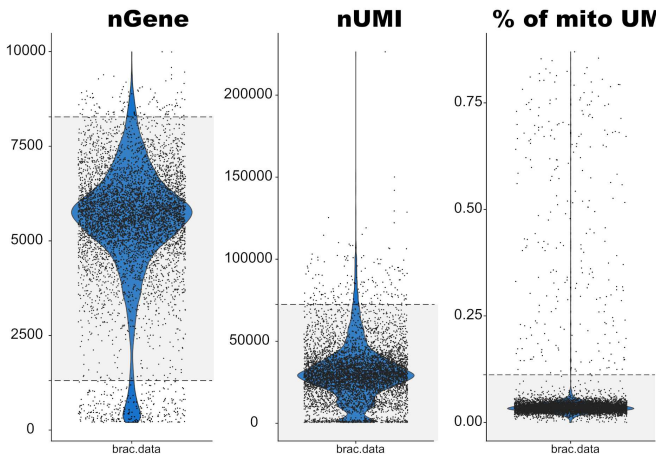
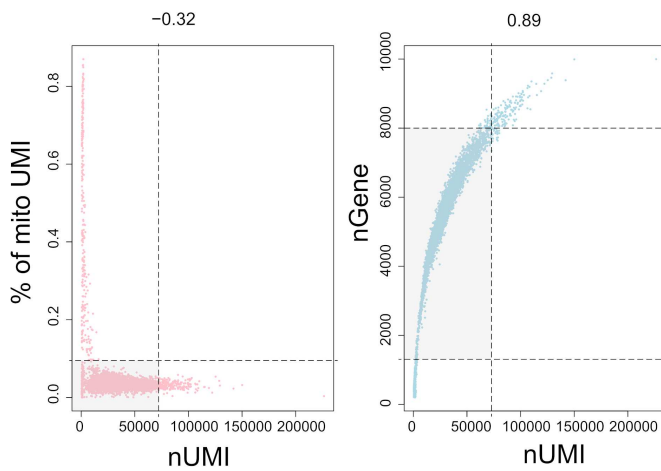
Schematic illustration of the juxtaposed positioning of cervical segments in Figure 1 and S1B. (B)

Immunostainings of Hoxa5 and Hoxc8 reveal the lineage segregation and boundary sharpening process between E11.5 and E12.5. Longitudinal sections of the spinal cord in which dorsal root ganglia were preserved were used to determine positions of cervical segments. Arrowhead indicates co-expression of Hoxa5 and Hoxc8 proteins at E11.5. Scale bar represents 100  $\mu$ m.

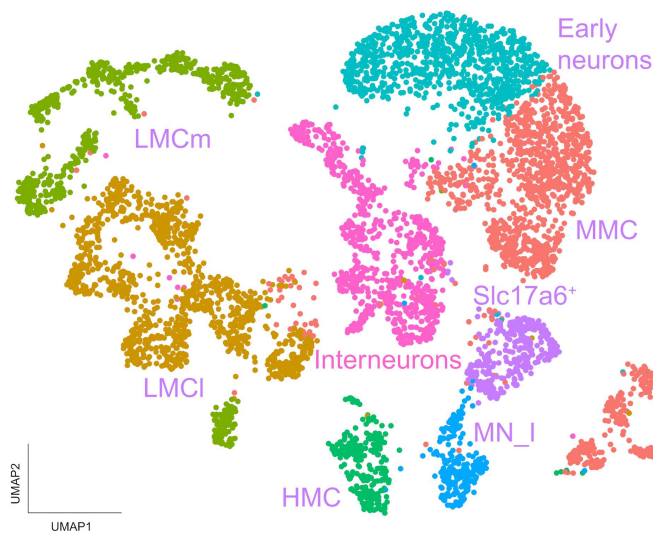
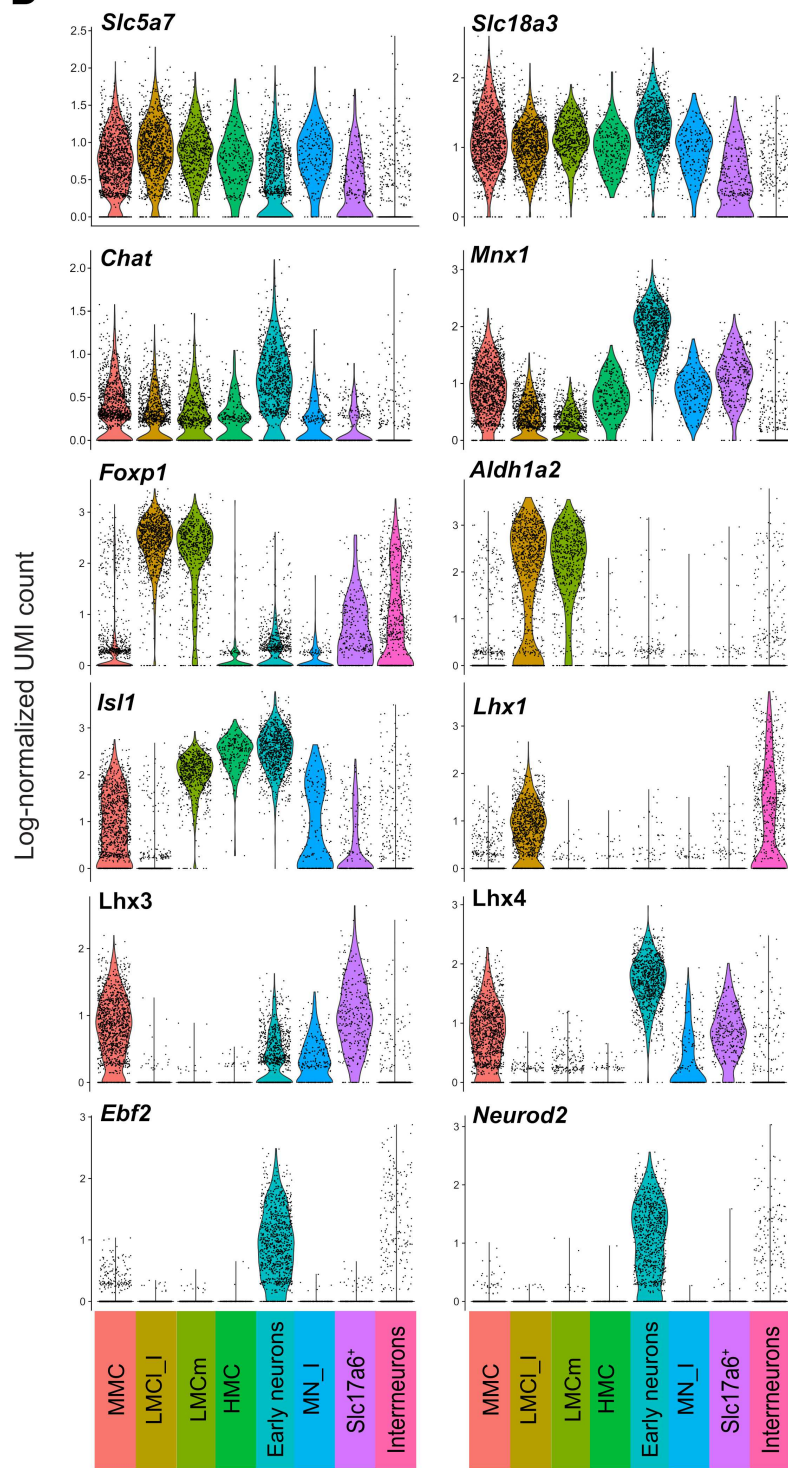
Figure S2

**A****T-UR Model****B****C****D****E****F**

**Figure S2. Transcriptional unilateral repression (T-UR) Model.** (A) Network diagram of the T-UR Model. Unlike the T-CR Model, regulation in this model is supported by experimental data. The T-UR Model was simulated in the same way as for the T-CR Model (Figure 2), including an assumed time-course of RA and FGF signaling at multiple locations along the rostrocaudal axis. (B) Simulation of the T-UR Model. A grid of 10X40 cells was used to represent a segment of developing spinal cord where progenitor cells are influenced by competing FGF and RA concentrations. Heatmaps show final distributions of denoted molecules in the tissue domain. Bottom panel shows the distribution of ratios between Hoxa5 and Hoxc8 protein levels. (C) Steady state levels of Hoxa5 and Hoxc8 proteins across RC domains. Error bar indicates 95% confidence interval for each position receiving the same amount of morphogen. (D) Bifurcation analysis with position as the control parameter. Solid curves denote stable steady states. Black line represents the steady state of the T-UR Model. Dashed curves denote unstable steady states. Other lines represent the steady states of the T-CR Model. Red:  $\text{Hoxa5}^{\text{on}}\text{Hoxc8}^{\text{off}}$  state; Green:  $\text{Hoxa5}^{\text{off}}\text{Hoxc8}^{\text{on}}$  state. The identities of these states were determined by protein levels, which are equivalent to free mRNA levels. (E) Distributions of transition widths from simulations with 10000 parameter sets for each of the T-CR and T-UR Models. Parameter sets with transition widths <10 are shown. (F) Network diagram of a system incorporating hypothetical positive feedbacks upstream of Hoxa5 and Hoxc8 via transcriptional control. Dashed lines represent hypothetical (unvalidated) regulations that may improve lineage segregation performance. Hoxa5 and Hoxc8 self-activation is also considered one type of hypothetical positive feedback.

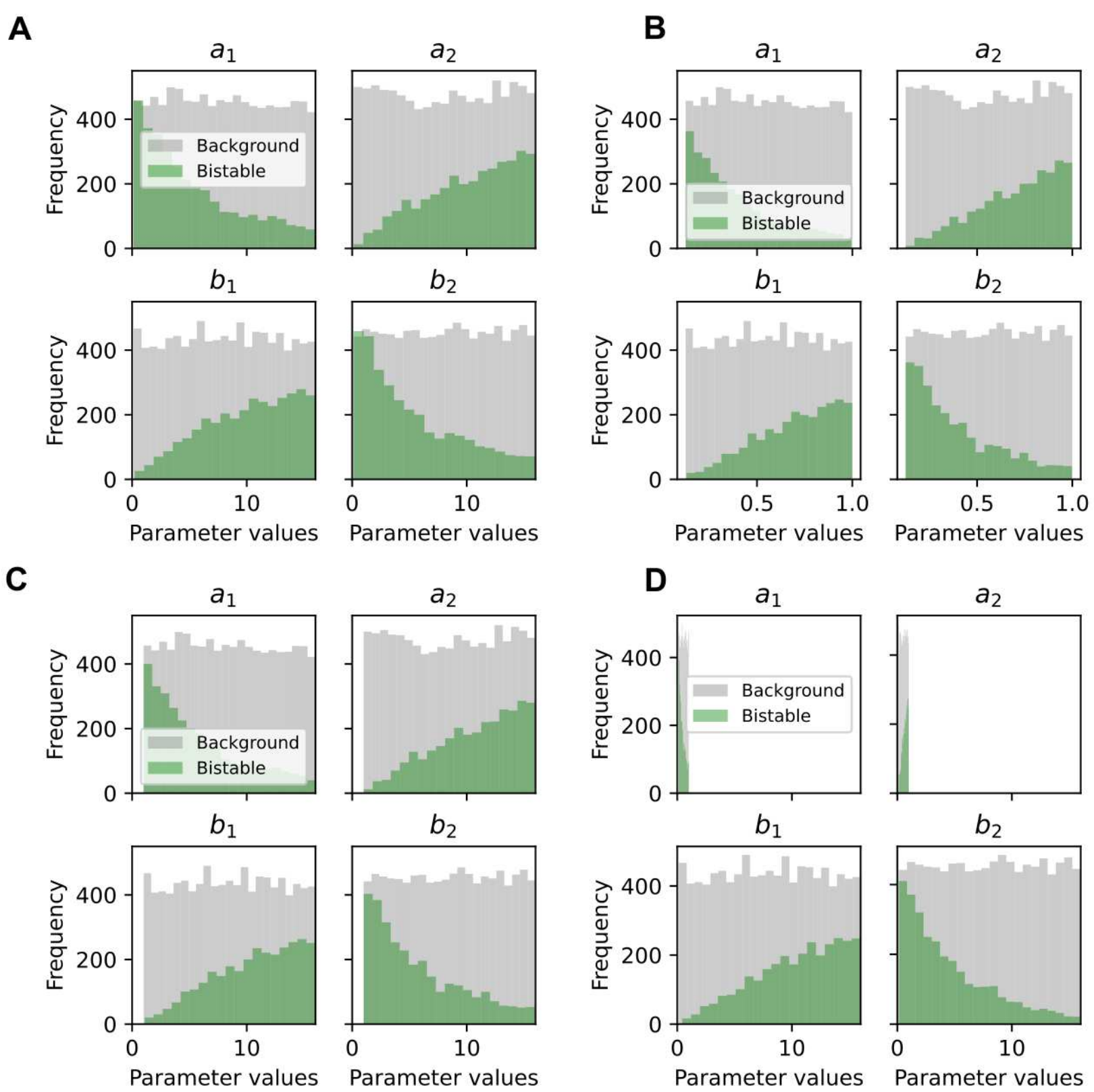
**A**Figure S3**B****C**

E12.5 cervical motor neuron sample

**D**

**Figure S3. Quality assessment and clustering analysis of collected E12.5 spinal motor neurons.** (A) Violin plot reflecting the number of expressed genes (nGene), unique molecular identifier counts (nUMI), and percentage of UMIs for mitochondrial genes for the collected single cells. (B) Scatter plot depicting the relationship between the features in (A) for quality filtering. Cells expressing fewer than 1300 genes and with more than 10% of UMI counts related to mitochondrial genes were excluded from downstream analyses. Dashed lines indicate the filtering cutoffs. (C) UMAP plot of 5581 cells upon quality filtering. Each cell is color-coded based on clustering results using a Louvain-Jaccard algorithm. Identities are assigned according to the expression of known MN markers as presented in (D). The eleven identified major clusters mainly comprised brachial LMC and MMC MNs based on prior experience (see Materials & Methods and SI Text for details).

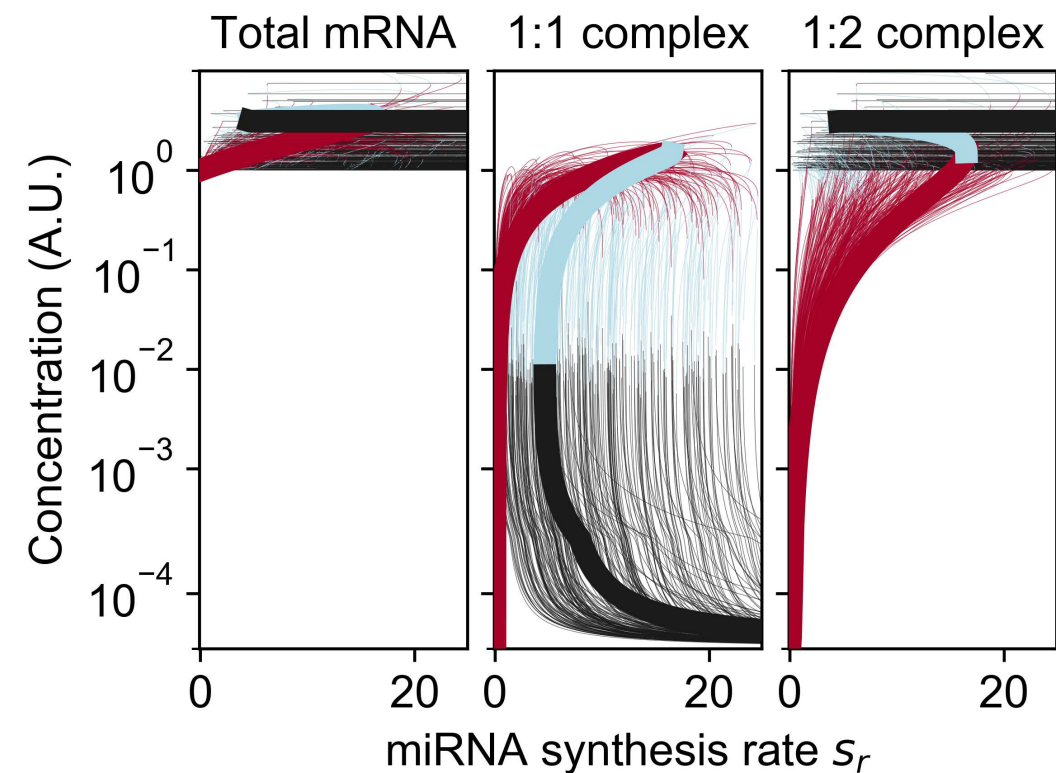
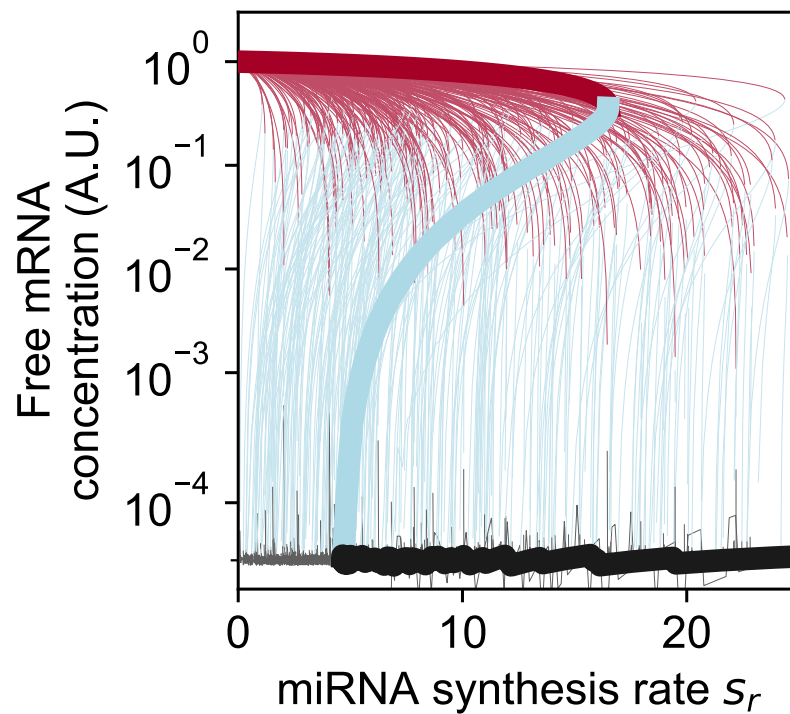
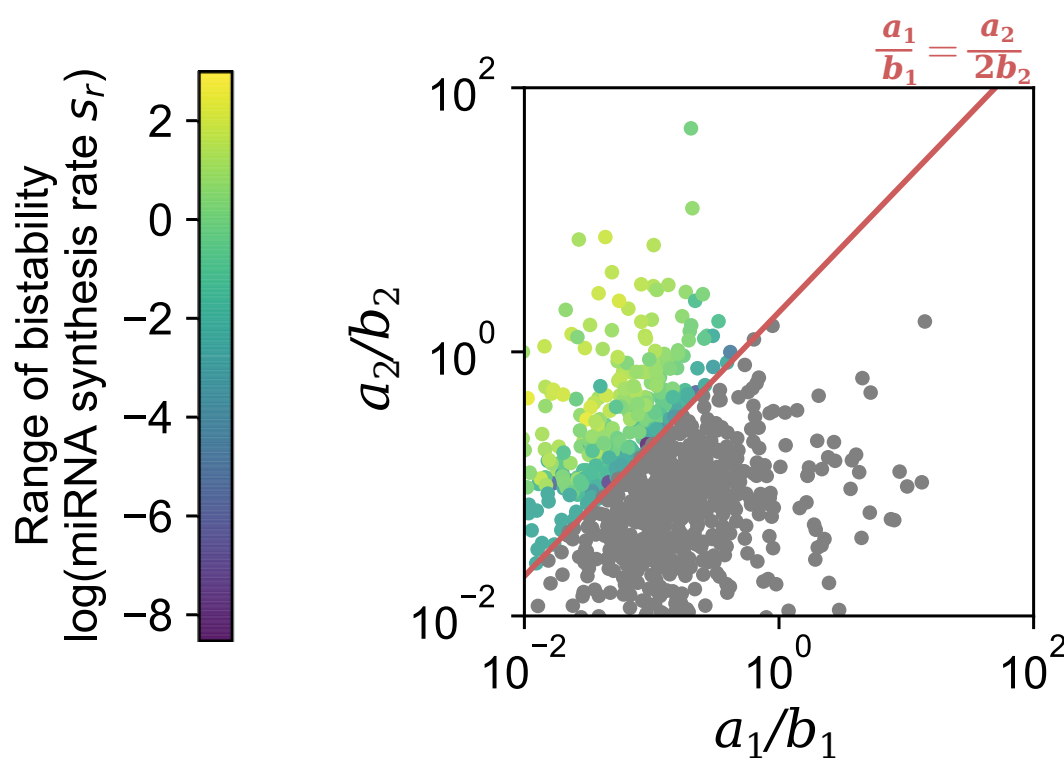
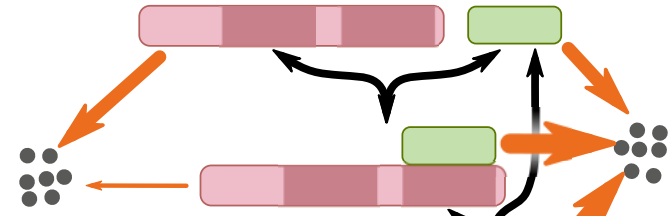
Figure S4



**Figure S4. Distributions of parameter values for bistable systems generated under the mmi-**

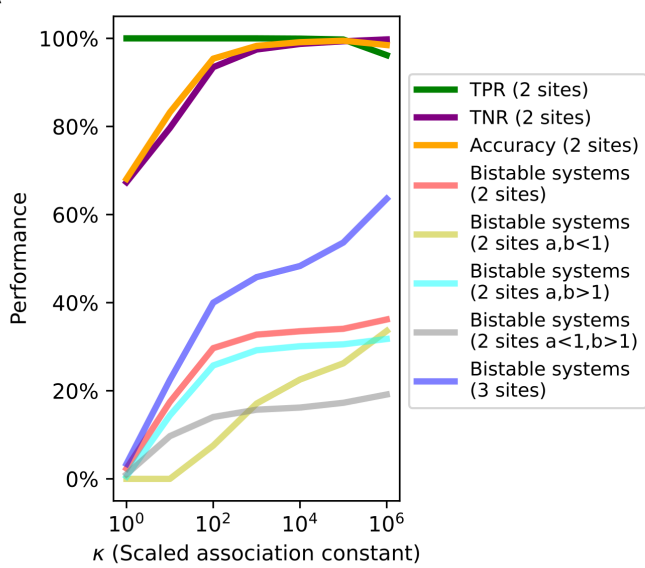
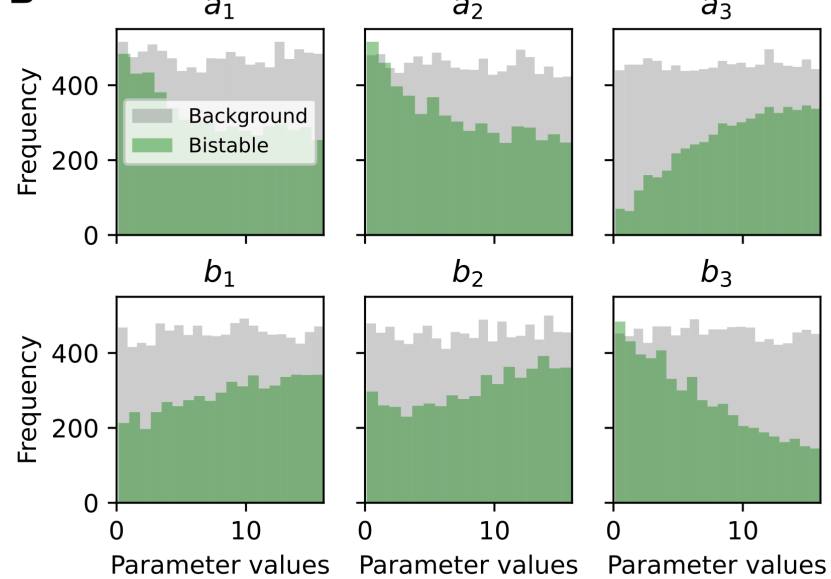
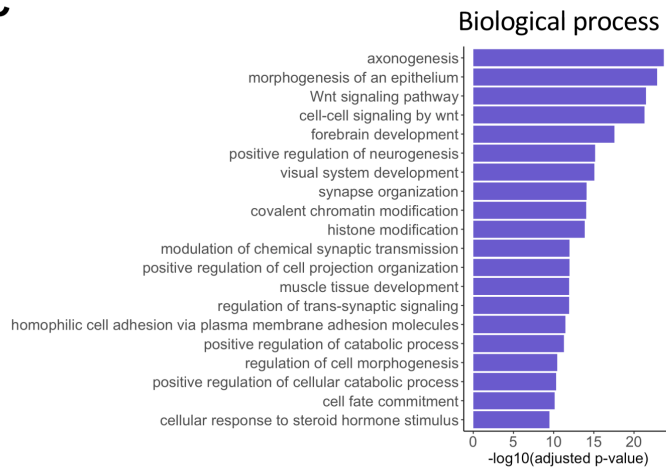
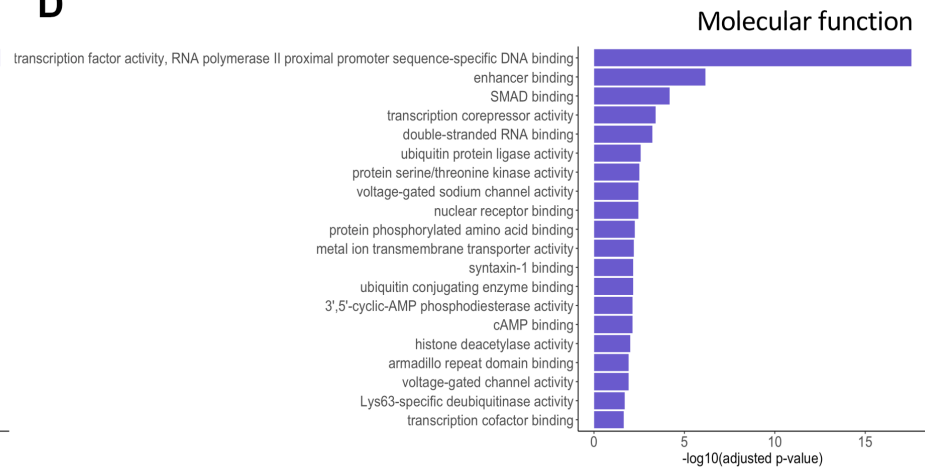
**2 Model.** Distributions of randomly selected parameter values for four scaled degradation rate constants (gray) under the mmi-2 Model, as well as the subset that generated bistable systems (green). Each of the 10000 randomly selected parameter sets was tested for bistability by means of numerical bifurcation analysis under a basal parameter setting ( $\gamma = 1, \kappa = 10^5$ ). Values of the four parameters were randomly drawn from uniform distributions over the intervals (0.125, 16) (A), (0.125, 1) (B), and (1, 16) (C). In panel (D), values for  $a_1$  and  $a_2$  were randomly drawn from a uniform distribution over the interval (0.125, 1), and values for  $b_1$  and  $b_2$  were randomly drawn from a uniform distribution over the interval (1, 16).

Figure S5

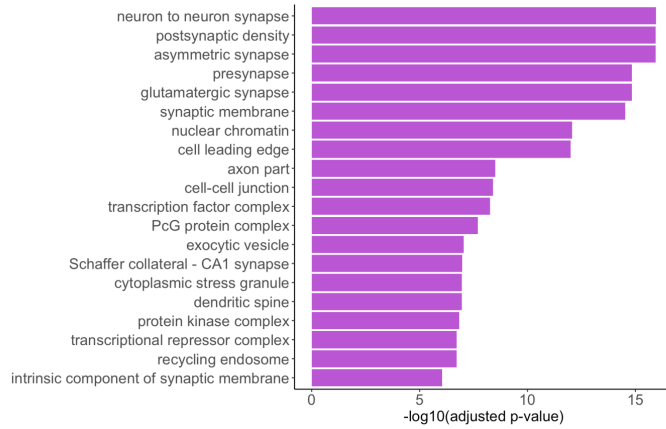
**A****B****C**

**Figure S5. Bistable systems generated from disproportionate degradation rate constants of miRNA and mRNA.** With the mmi-2 Model, we generated 10000 parameter sets with values for  $a_1$  and  $a_2$  randomly drawn from a uniform distribution over the interval (0.125, 1), and for  $b_1$  and  $b_2$  randomly drawn from a uniform distribution over the interval (1, 16). All other parameters, except the control parameter for bifurcation analysis and the scaled dissociation rate constant ( $Kk_R^0/s_R = 10^{-5}$ ), were set to 1. (A) Bifurcation diagrams show steady states calculated for 3348 bistable systems out of 10000 parameter sets. Red curve: stable steady state with high amounts of free mRNA. Black curve: stable steady state with low amounts of free mRNA. Blue curve: unstable steady state. One representative system is highlighted with thick curves, and the other systems are depicted with thin curves. (B) Stability properties of the 10000 randomly generated systems. Monostable systems (gray dots) and bistable systems (purple-green dots) are shown in the dimensions of  $a_1/b_1$  and  $a_2/b_2$ . The color gradient denotes the range of bistability in terms of the control parameter. Orange dot denotes the condition under which degradation of mRNA and miRNA is balanced in both complexes. Red line is the threshold for bistability predicted by analytical methods. (C) Network diagram of a mmi-2 Model with arrows representing bistability-enabling parameters described in A and B.

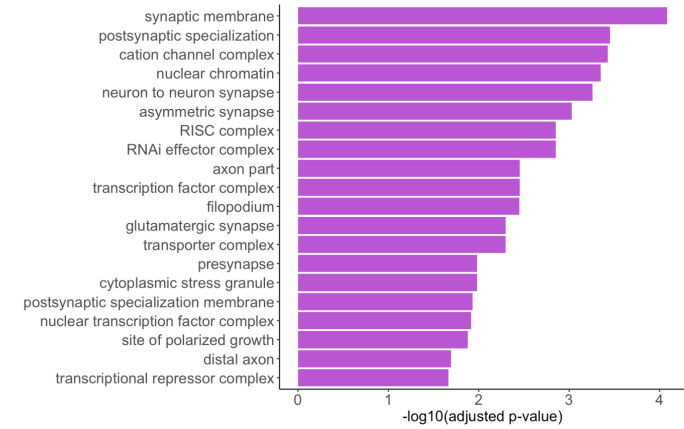
Figure S6

**A****B****C****D**

Cellular component



Cellular component

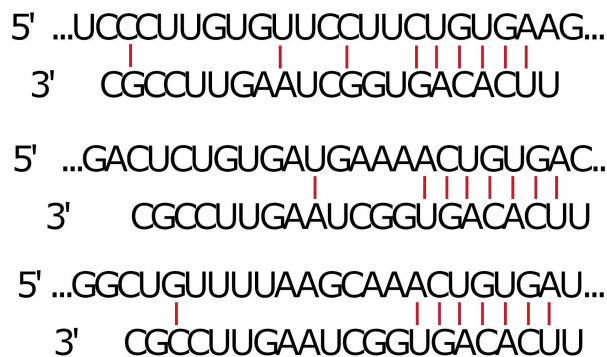
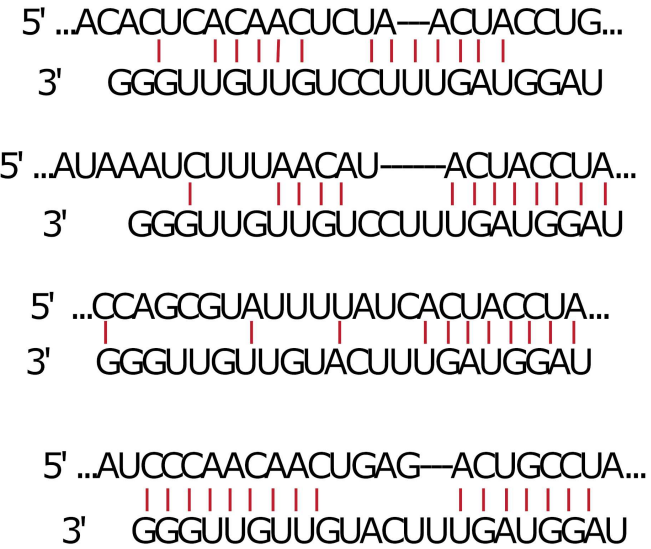
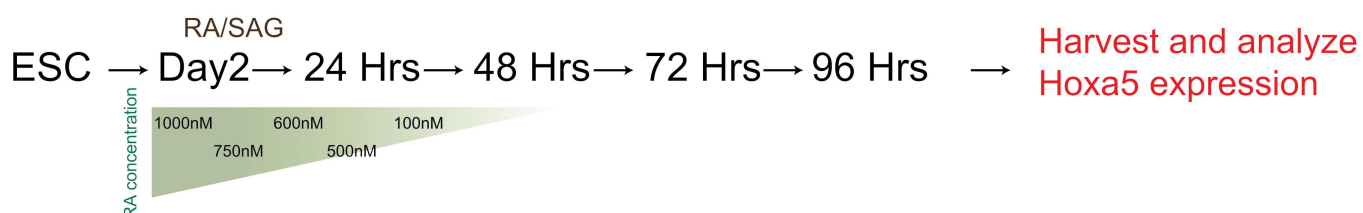
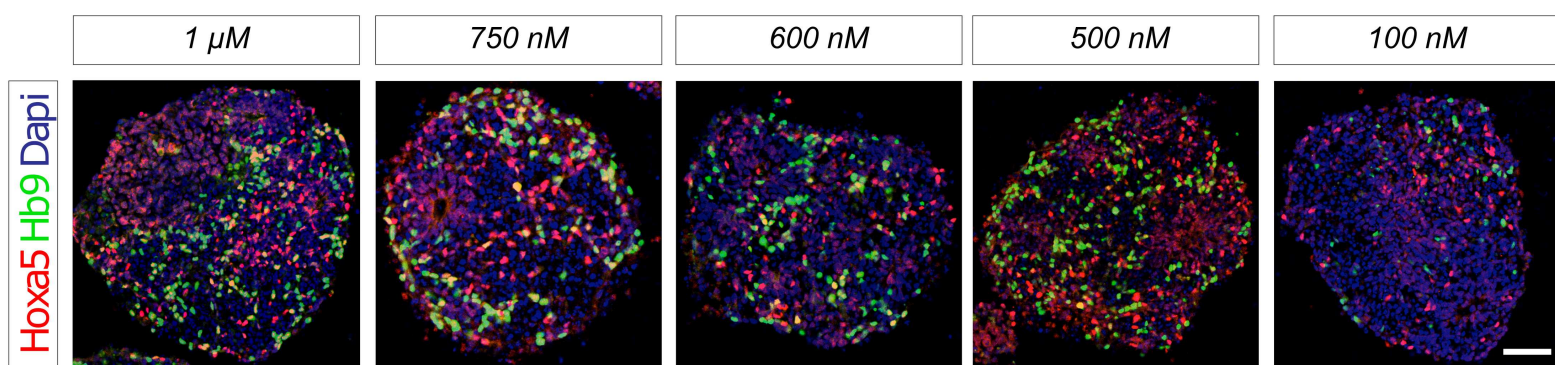
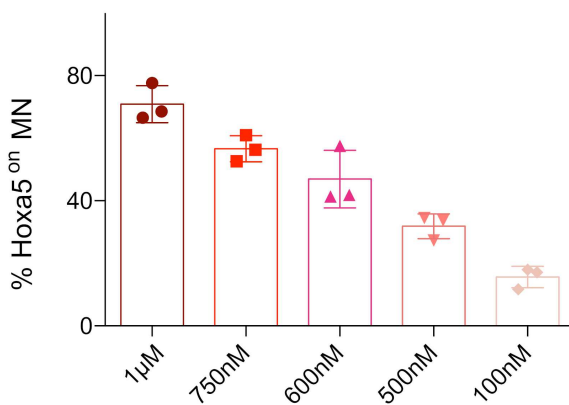


**Figure S6. Performance of analytical predictions for bistable systems under various models and distributions of parameters values for bistable systems generated with the mmi-3 Model.**

(A) The three top lines of the graph show the performance (TPR: true positive rate; TNR: true negative rate; and accuracy) of Eq 1 in predicting the bistability of the mmi-2 model. Other lines show the fractions of bistable systems with various constraints of parameter sampling, model choice, and values of  $\kappa$ . (B). Distributions of randomly selected parameter values for six scaled degradation rate constants (gray) under the mmi-3 Model and the subset that generated bistable systems (green). Each of the 10000 randomly selected parameter sets was tested for bistability by numerical bifurcation analysis under a basal parameter setting ( $\gamma = 1, \kappa = 10^5$ ). Values of the four parameters were randomly drawn from uniform distributions over the intervals (0.125, 16).

(C) Gene ontology enrichment analysis for miRNA targeted genes with 2 or more binding sites and (D) 3 or more binding sites. Bar plot shows the top 20 significant terms related to biological process or molecular function (top) and cellular component (bottom).

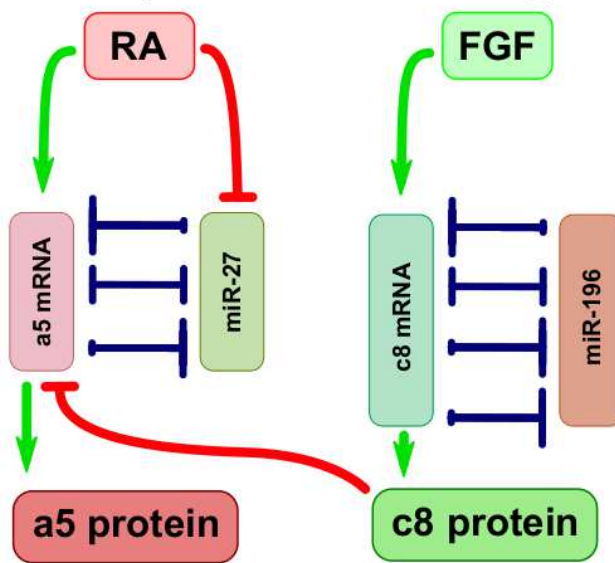
Figure S7

**A****miR-27 Hoxa5****miR-196 Hoxc8****B****C****D**

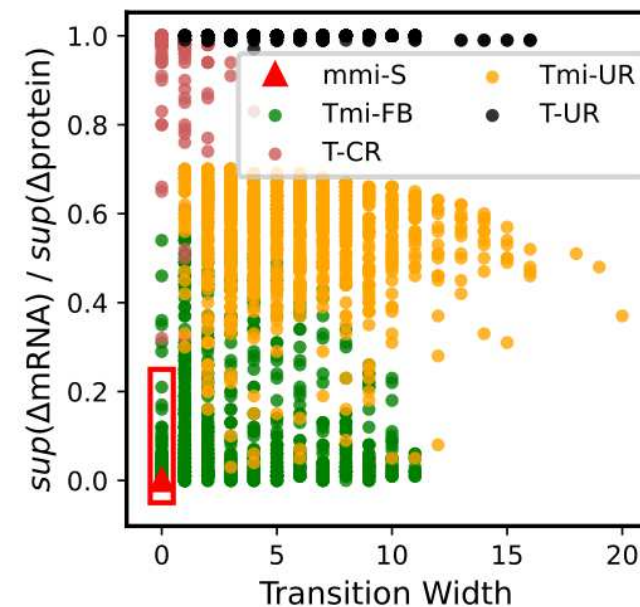
**Figure S7. A gradient of RA gives rise to proportional Hoxa5<sup>on</sup> cell counts upon ESC differentiation.** (A) Predicted targeting sites for *miR-27* in the *Hoxa5* 3' UTR (left panel) and for *miR-196* in the *Hoxc8* 3' UTR (right panel), based on TargetScan. (B) Schematic illustration of the experiments in (C) and (D). (B) Immunostainings of Hoxa5 and Hb9 in embryoid bodies with a concentration gradient of RA ranging from 100 nM to 1  $\mu$ M. (D) Quantification of Hox5<sup>on</sup> cells from the Hb9<sup>on</sup> population. Scale bar in (C) represents 50  $\mu$ m. Data in (D) represent mean  $\pm$  SD, N $\geq$ 3 EBs from three independent experiments.

Figure S8

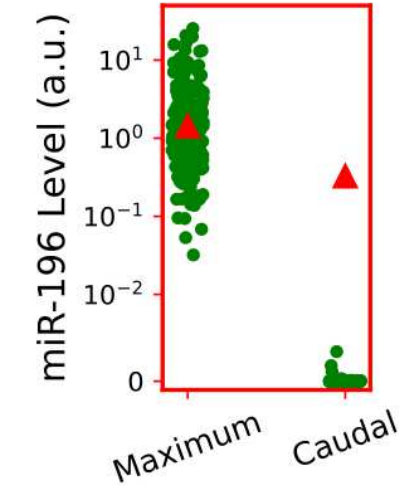
# A mmi-S (influence diagram)



# B

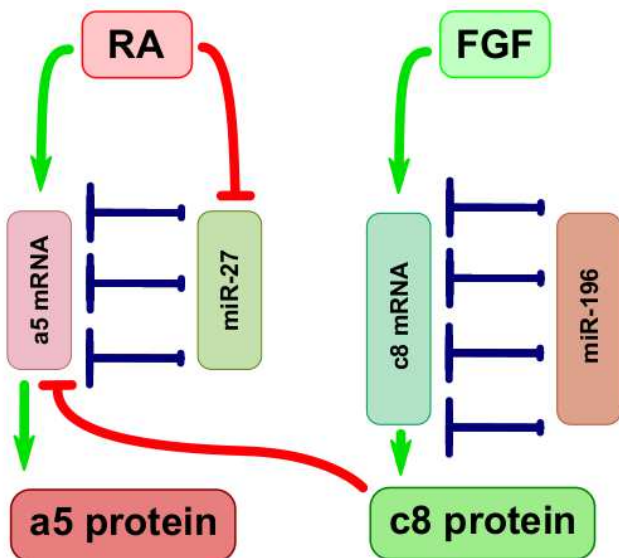


# C



# D

## Altered mmi-S



# E

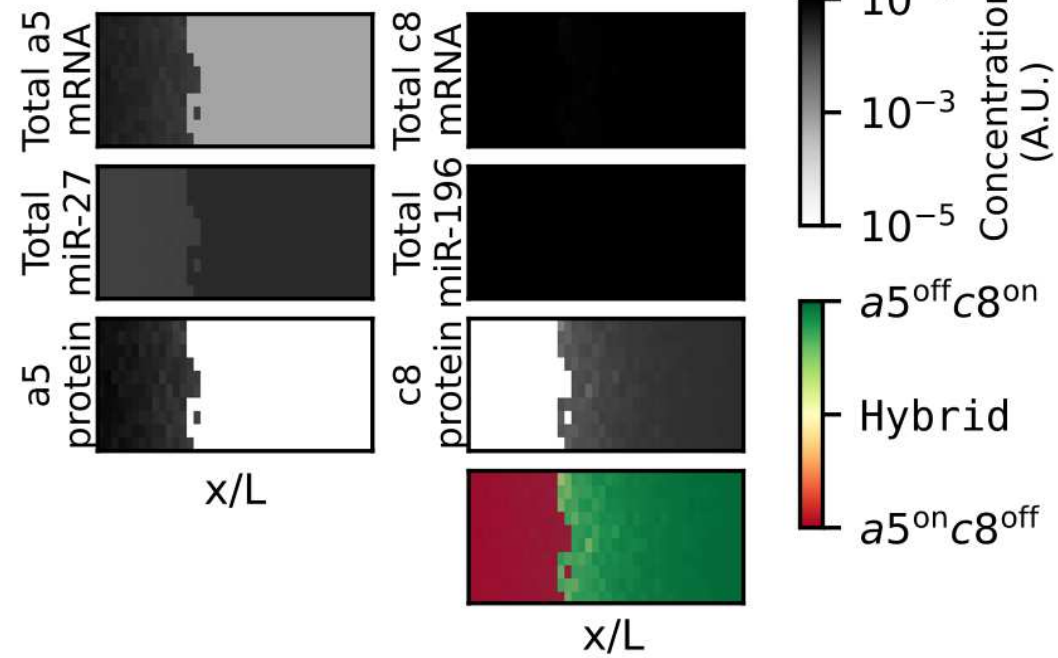


**Figure S8. Performance and perturbation of the mRNA-miRNA feedback.** (A) Influence diagram of the feedback loops in the mmi-S Model (Figure 8A). (B) Performance of the mmi-S Model overlaid with that of four other models presented in Figure 4G. (C) Performance of the mmi-S Model overlaid with that of the Tmi-FB Model presented in Figure 4H. (D) Influence diagram of an altered mmi-S Model exhibiting unidirectional regulation of mRNA by miRNA, which does not allow feedback formation. Only intracellular parts of the models are shown. (E) Tissue domain patterning at the final time point for the altered mmi-S Models.